Characterization of Cement-Based Multiphase Materials Using Ultrasonic Wave Attenuation

A Thesis
Presented to
The Academic Faculty

by

Martin Treiber

In Partial Fulfillment
of the Requirements for the Degree
Master of Science in Engineering Science and Mechanics

School of Civil and Environmental Engineering
Georgia Institute of Technology
December 2008

Characterization of Cement-Based Multiphase Materials Using Ultrasonic Wave Attenuation

Approved by:

Dr. Laurence J. Jacobs, Advisor
School of Civil and Environmental Engineering
Georgia Institute of Technology

Dr. Jin-Yeon Kim
School of Civil and Environmental Engineering
Georgia Institute of Technology

Dr. Jianmin Qu
George W. Woodruff School of Mechanical Engineering
Georgia Institute of Technology

Date Approved: August 22, 2008

To my family and friends
who make me who I am

ACKNOWLEDGEMENTS

This work would not have been possible without the support from a number of people who encouraged me during my stay in the United States.

Most importantly, I would like to thank Prof. Laurence 'Larry' Jacobs for being an outstanding advisor, teacher, and friend, supporting me in an unprecedented way during my stay at Georgia Tech.

For his sharing of knowledge and the encouragement during the whole research, especially in the challenging phases of the project, I express my gratitude to Dr. Jin-Yeon Kim.

Special thanks also go to Dr. Jianmin Qu for being a great teacher, and for his helpful advice during the work on this thesis.

I am deeply indebted to Prof. Dr.-Ing. Lothar Gaul and the Institut für Angewandte und Experimentelle Mechanik for enabling me to live this unique experience by establishing this great exchange program. The generous financial and organizational support provided by the German Academic Exchange Service (DAAD) is greatly appreciated.

I would like to express my sincere gratefulness to all my friends who contributed in an invaluable way in making this year an unforgetable experience. Specifically, I thank Aline 'Dobby' Zimmer for her support during the last year. I thank my labmates Michael Braun, Richard Kmack, and Christoph Prüll for the fruitful discussions, the enjoyable atmosphere in the lab, and the fun we had together.

Finally, I express my loving gratefulness to my family who has always encouraged me in all my adventures. Your love and support have brought me to where I am and I cannot express my thankfulness for your enduring belief in me and my future.

TABLE OF CONTENTS

LIST OF TABLES

LIST OF FIGURES

LIST OF SYMBOLS OR ABBREVIATIONS

ASR	Alkali-silica reaction
FFT	Fast Fourier transformation
NDE	Nondestructive evaluation
PDE	Partial differential equation
SHM	Structural health monitoring
SNR	Signal to noise ratio
$\lvert\cdot\rvert$	Magnitude
$\arg(\cdot)$	Unwrapped phase of complex value
$\tilde{\cdot}$	Complex value
∇	Nabla operator
a	Scatterer (inclusion) radius
A	Amplitude
b	Transducer radius
c, c_{L}, c_{S}	Wavespeeds
$\mathbf{d}$	Vector of particle displacement direction
$D(\xi)$	Diffraction coefficient
E	Young's modulus
$\bar{\mathbf{e}}_{\mathbf{r}}$	Unit vector in radial direction

f	Frequency
f_l	Body force
$h_m(\xi)$	Spherical Bessel function of the third kind and order m
i	Imaginary unit
$j_m(\xi)$	Spherical Bessel function of the first kind and order m
k, k_l, k_s	Wave numbers
M1, M2, ... M6	Measurement steps
n_s	Number of scatterers
$P_m(\xi)$	Legendre polynomial of degree m
$\mathbf{p}$	Vector of propagation direction
R	Reflection coefficient
S_1, S_2	Reflected or transmitted signals
t	Temporal variable
T	Transmission coefficient
u	Particle displacement
x, x_1, x_2, $\mathbf{x}$	Spatial variables
z	Specimen thickness
α	Attenuation coefficient
γ^{sca}	Scattering cross-section
δ_{ij}	Kronecker delta
ϵ_{ij}	Strain tensor
η	Volume fraction of elastic inclusions

κ	Bulk modulus
λ, μ	Lamé's constants
Λ	Wavelength
ν	Poisson's ratio
ρ	Density
σ_{ij}	Stress tensor
ϕ	Volume fraction of cavities
φ	Scalar potential
$\boldsymbol{\varphi}$, $\boldsymbol{\Psi}$, $\boldsymbol{\Pi}$	Vector potentials
ω	Circular frequency

SUMMARY

Ultrasonic wave attenuation measurements have been used to successfully characterize the microstructure and material properties of inhomogeneous materials; these ultrasonic techniques have the potential to provide for the in situ characterization of heterogeneous, cement-based materials. Recent research has applied existing acoustic scattering models to predict ultrasonic attenuation in relatively simple cement-based materials with good results. The goal of the current research is to extend this past work and to investigate the influence of elastic inclusions in order to simulate a more realistic microstructure: a cement paste matrix material that contains both sand inclusions and air voids. The sand inclusions simulate fine aggregates as they are present in real civil engineering structures, while the air voids provide an additional microstructure that is present in concrete components. This research considers an independent scattering model as well as a self-consistent effective medium theory approach in order to model the scattering attenuation due to the sand inclusions in the cement paste matrix. The research develops a reliable measurement technique essential to assess the wave attenuation of the particulate materials. Subsequently, the ultrasonic wave attenuation is measured in cement paste specimens of various types. The measured attenuation is then compared to the model predictions and the results are discussed. Finally, theoretical approaches to model the described three-phase materials are presented and discussed.

CHAPTER I

INTRODUCTION

Concrete and other cement-based materials define a major component of the materials used in civil engineering applications such as buildings, bridges, roads and other transportation infracstructure. Today, concrete is by volume the largest manufactured product in the world [19].

In spite of the apparent simplicity of the production technology, the microstructure of cement-based materials is highly complex. Nevertheless, the knowledge of the microstructure allows for the characterization of the material performance on a macroscale and for the monitoring of structural health.

In the past decades, ultrasonic testing techniques have shown the capability to characterize material performance and are therefore commonly used in current nondestructive evaluation (NDE) procedures. For cement-based materials, ultrasonic testing techniques and specifically attenuation measurements have been successfully employed to characterize the microstructure of different materials with good results. These techniques have the potential for the utilization in NDE applications and can later be used to implement a complete structural health monitoring (SHM) system into civil engineering components.

On the other side, researchers have developed a large number of different modeling techniques, in order to predict the acoustic behavior of several materials. These models have been applied to different applications of wave propagation and have shown good agreement with measurement data. Hence, in combination with measurements, these models can be applied in inverse problems to allow for the characterization of

material properties and performance.

In recent studies, ultrasonic wave attenuation measurement and modeling techniques have been successfully applied in order to characterize air voids attendant in cement paste with no further inclusions [26, 27]. Air voids play an important role in freezing and thawing mechanisms whose effects can give rise to microcracks that deteriorate the material's performance. The in-situ quality control and health monitoring of civil engineering infrastructure are thereby essential for the construction industry. The question if the characterization techniques for air voids are still applicable in a more realistic model of real concrete that includes coarse aggregates is therefore of specific interest. In order to investigate this issue, it is crucial to gain a fundamental understanding of how the coarse aggregates as they are present in real structures influence the propagation and attenuation of ultrasonic waves. Moreover, an expanded knowledge of the general mechanisms of propagation and scattering of waves in viscoelastic materials can be applied to further application in science and engineering.

The objective of this research is to investigate the influence of sand inclusions in a cement paste material on the attenuation of longitudinal ultrasonic waves of wavelengths that are comparable to the length scale of the material's microstructure. Different modeling approaches are applied to this specific combination of materials and their respective results are compared to each other in order to define which models are suitable to characterize the measured material behavior.
A measurement technique for highly attenuative, particulate materials is developed and employed on cement paste and mortar specimens with varying amounts of sand inclusions in order to measure the wave attenuation in a high frequency range.
Finally, the measured attenuation is compared to the different model predictions and the accuracy of the respective models is evaluated.

First, this thesis gives a short introduction to the fundamental theory of wave propagation and describes important wave phenomena as they relate to the current research. Next, the basic ideas of the two modeling approaches for wave attenuation are provided and their results are depicted. Subsequently, the proposed measurement technique is explained and its accuracy and robustness is demonstrated on a reference specimen. A description of the cement-based materials specimens and their properties follows before the measurement results are presented. Finally, these results are compared to the model predictions and the relationship is interpreted. Modeling techniques and combinations are provided to model a three-phase material. The thesis ends with a concluding summary and provides an outlook as well as an overview of the further work to be conducted.

CHAPTER II

THEORETICAL BACKGROUND

In this chapter, the fundamental theory of wave propagation in linear materials as well as some important wave phenomena such as reflection and attenuation are described. The governing equations of wave motion are derived and their basic solutions for specific boundary conditions are provided. Mathematical descriptions for reflection and attenuation are discussed.

Further information on the topic of wave propagation can be found in numerous sources such as [1, 7].

2.1 Linear Wave Propagation

In the theory of linear elasticity, the traction t_i on a plane described by $n_i x_i = d$ is given by

$$t_i = \sigma_{ij} n_j \,, \tag{2.1}$$

where the stress tensor is denoted by σ_{ij}.

For the derivation of the equations of motion, an arbitrarily shaped body of volume V bounded by the surface S as in Figure 2.1 is considered. The balance of linear

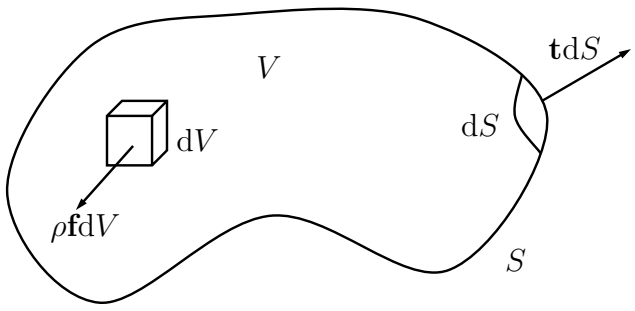

Figure 2.1: Momentum balance

momentum can then be expressed as

$$\int_S \sigma_{kl} n_k \mathrm{d}S + \int_V \rho f_l \mathrm{d}V = \int_V \rho \ddot{u}_l \mathrm{d}V \,, \tag{2.2}$$

where ρ represents the material mass density and f_l the body force. Gauss's theorem applied to Eq. 2.2 yields

$$\int_V \left(\sigma_{kl,k} + \rho f_l - \rho \ddot{u}_l\right) \mathrm{d}V = 0 \,. \tag{2.3}$$

Since the body may have an arbitrary shape, it follows that for a continuous integrand

$$\sigma_{kl,k} + \rho f_l = \rho \ddot{u}_l \tag{2.4}$$

has to be satisfied. This relationship is called Cauchy's first law of motion.

Eq. 2.4 contains terms of stress σ_{ij} and displacement u_i. Generally, a more convenient form of representing the equations of motion solely in terms of the field function u_i can be found by applying Hooke's law for a homogeneous, isotropic and linear elastic medium, which is given by

$$\sigma_{ij} = \lambda \epsilon_{kk} \delta_{ij} + 2\mu \epsilon_{ij} \,, \tag{2.5}$$

where λ and μ are the first order Lamé constants. The strain tensor ϵ_{ij} is related to the displacement u_i by

$$\epsilon_{ij} = \frac{1}{2}(u_{i,j} + u_{j,i}) \,. \tag{2.6}$$

Substitution of Eq. 2.6 into Eq. 2.5 and subsequently into Eq. 2.4 leads to Navier's formulation of the equations of motion

$$\mu u_{i,jj} + (\lambda + \mu) u_{j,ji} = \rho \ddot{u}_i \,, \tag{2.7a}$$

which reads in vector representation as

$$\mu \nabla^2 \mathbf{u} + (\lambda + \mu) \nabla \nabla \cdot \mathbf{u} = \rho \ddot{\mathbf{u}} \,. \tag{2.7b}$$

Notice that body forces f_i are neglected in this development.

For the three-dimensional case, Eqs. 2.7 represent a set of three coupled partial differential equations (PDE's) whose solution is generally difficult to obtain. However, the Helmholtz decomposition

$$\mathbf{u} = \nabla\varphi + \nabla \times \boldsymbol{\psi} \,, \tag{2.8}$$

provides a convenient way to uncouple these equations to yield a set of two PDE's. In this framework, Eq. 2.8 represents the three components of the displacement vector $\mathbf{u}$ with the potential functions φ, ψ_1, ψ_2 and ψ_3. To guarantee the uniqueness of the solution, the additional constraint

$$\nabla \cdot \boldsymbol{\psi} = 0 \tag{2.9}$$

is necessary.

Substitution of the Helmholtz decomposition into the governing Equations, Eqs. 2.7, leads to the above mentioned set of uncoupled PDE's in terms of the displacement potentials φ and $\boldsymbol{\psi}$:

$$\nabla^2\varphi = \frac{1}{c_{\mathrm{L}}^2}\ddot{\varphi} \,, \qquad \nabla^2\boldsymbol{\psi} = \frac{1}{c_{\mathrm{S}}^2}\ddot{\boldsymbol{\psi}} \,. \tag{2.10}$$

As will be shown later, c_{L} and c_{S} denote the phase velocities of a longitudinal and a vertically or horizontally polarized shear wave, respectively. These wave speeds are functions of the material properties only and are given by

$$c_{\mathrm{L}} = \sqrt{\frac{\lambda + 2\mu}{\rho}} \,, \qquad c_{\mathrm{S}} = \sqrt{\frac{\mu}{\rho}} \,. \tag{2.11}$$

As it can be seen from Eq. 2.11, it always holds true that the longitudinal wave is faster than the shear wave, i.e. $c_{\mathrm{L}} > c_{\mathrm{S}}$.

For convenience, the wave speeds are expressed in terms of the Lamé constants λ and μ. A relationship to the more commonly used material properties Young's modulus

E and Poisson's ratio ν is given by

$$\lambda = \frac{E\nu}{(1+\nu)(1-2\nu)}\,, \tag{2.12}$$

$$\mu = \frac{E}{2(1+\nu)}\,. \tag{2.13}$$

Furthermore, the bulk modulus κ is often found in the literature and will be used for some modeling that is described later. It is related to the Lamé constants as

$$\kappa = \lambda + \frac{2}{3}\mu\,. \tag{2.14}$$

2.2 Wave Phenomena

The wave phenomena discussed in the following sections are based on the plane wave assumption, that is, assuming a wave with constant properties (ϵ, σ, u) on a plane perpendicular to its propagation direction, $\mathbf{p}$. The mathematical representation of a plane wave is

$$\mathbf{u} = \mathbf{d}f(\mathbf{x}\cdot\mathbf{p} - ct)\,, \tag{2.15}$$

where $\mathbf{d}$ is the unit vector defining the direction of particle motion, c is either the longitudinal wave speed c_L or the shear wave speed c_S, and the function f is an arbitrary function that defines the shape of the travelling wave. It can easily be shown that any function of the form $f(\mathbf{x}\cdot\mathbf{p} - ct)$ satisfies the governing equations of motion, Eqs. 2.7.

Substitution of Eq. 2.15 into the equation of motion yields

$$(\mu - \rho c^2)\mathbf{d} + (\lambda+\mu)(\mathbf{p}\cdot\mathbf{d})\mathbf{p} = \mathbf{0}\,. \tag{2.16}$$

The two types of waves that form the basis of the wave propagation theory are obtained by the two possible solutions of the above equation. Since $\mathbf{p}$ and $\mathbf{d}$ are different unit vectors, either $\mathbf{d} = \pm\mathbf{p}$ or $\mathbf{p}\cdot\mathbf{d} = 0$ are possible solutions:

1) $\mathbf{d} = \pm\mathbf{p}$ leads to $\mathbf{p}\cdot\mathbf{d} = \pm 1$. Inspection of Eq. 2.16 yields $c = c_\mathrm{L}$ as defined in Eq. 2.11. Furthermore, $\mathbf{d}$ and $\mathbf{p}$ are linearly dependent which represents a

particle movement in the direction of propagation $\mathbf{p}$ and therefore describes a longitudinal or pressure wave (P-wave).

2) $\mathbf{p} \cdot \mathbf{d} = 0$ leads to $c = c_{\mathrm{S}}$ as defined in Eq. 2.11. Thus, the direction of particle motion is normal to the direction of propagation. That describes a shear wave (or transverse wave). If a two-dimensional plane of propagation in the x_1, x_2-plane is considered, a wave with an in-plane displacement is called a vertically polarized shear wave or SV-wave, while a wave with out-of-plane displacement is called a horizontally polarized wave or SH-wave.

2.2.1 Harmonic Waves

In the theory of plane waves described above, the shape of the travelling waveform $f(\mathbf{x} \cdot \mathbf{p} - ct)$ can be of arbitrary form.
However, specifically important are waveforms of the form

$$u(x,t) = A \cos\left[\omega(\frac{x}{c} - t)\right] \tag{2.17}$$

with amplitude A and circular frequency ω. These waves show a harmonic behavior in time and space and are discussed for the one-dimensional case in the following.
For mathematical simplicity, Eq. 2.17 is often written using the complex exponential expression

$$u(x,t) = A\, e^{i(kx-\omega t)}\,, \tag{2.18}$$

where

$$k = \frac{2\pi}{\Lambda} = \frac{\omega}{c} \tag{2.19}$$

denotes the wavenumber of the harmonic wave of wavelength Λ. The term $(kx - ct)$ is often refered to as the phase of the wave.

In homogeneous, isotropic materials, longitudinal and shear phase velocities c_{L} and

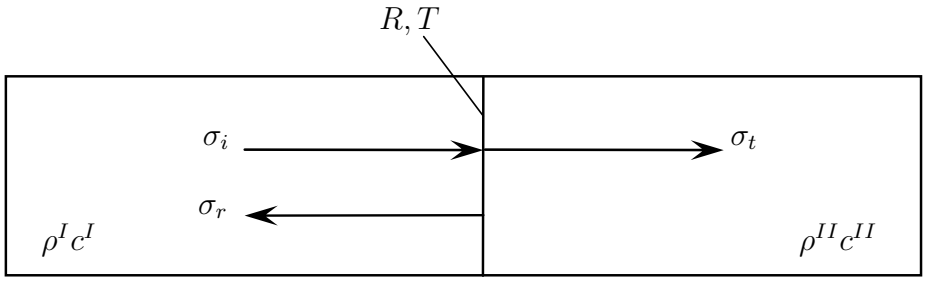

Figure 2.2: Reflected and transmitted waves

c_S are not a function of the circular frequency ω. Nevertheless, in more complex materials, this is not the case any more and a dispersion-relationship between frequency and phase velocity has to be found. These media are called dispersive.

2.2.2 Reflection and Transmission of One-dimensional Waves

Reflection and transmission of travelling disturbances in a material occur if the wave strikes an ideal interface of two elastic media with different acoustic properties. Specifically, these properties are described by the acoustic impedance ρc, which is defined as the product of density and phase velocity for the type of wave considered. Any missmatch in the impedance of two joined materials gives rise to a reflected and a transmitted portion of the incident wave, see Figure 2.2.

As it is known from the theory of wave propagation, the incident wave σ_i can be written in the following fashion [1]:

$$\sigma_i = f(t - \frac{x}{c}) \,. \tag{2.20}$$

The reflected and transmitted waves can be expressed in terms of the incident wave as

$$\sigma_r = R\, f(t - \frac{e}{c} + \frac{x - e}{c}) \,, \tag{2.21}$$

and

$$\sigma_t = T\, f(t - \frac{e}{c} - \frac{x - e}{c}) \,, \tag{2.22}$$

where R and T denote the reflection and transmission coefficient, respectively and e defines the propagation distance to the interface. From the continuity condition of stress and displacement at the interface, these coefficients are found to be

$$R = \frac{\rho^{II}c^{II}/\rho^{I}c^{I} - 1}{\rho^{II}c^{II}/\rho^{I}c^{I} + 1}\,, \tag{2.23}$$

and

$$T = 2\frac{\rho^{II}c^{II}/\rho^{I}c^{I}}{\rho^{II}c^{II}/\rho^{I}c^{I} + 1}\,. \tag{2.24}$$

From the definition of R and T it follows that $-1 \leq R \leq 1$ and $0 \leq T \leq 2$.

Specifically important is the case of a free surface where the adjacent media cannot carry any mechanical waves, i.e. $\rho^{II}c^{II} \to 0$. In this case the reflected wave has the same shape as the incident one but the sign of the stress changes upon reflection. Thus, the reflection- and transmission coefficients take the valus $R = -1$ and $T = 0$.

2.2.3 Reflection of Two-dimensional P and SV-Waves

In an unbounded, infinite media, the above mentioned waves propagate independently. Reflections and coupling of P- and SV-waves occur on interfaces of materials with different acoustic properties in which the waves propagate. These interface reactions can be found at the boundaries of a finite media.

An incident P-wave (SV-wave), which is reflected at a stress free boundary (i.e. $\sigma_{21} = \sigma_{22} = 0$) normally consists of both, a P-wave (SV-wave) and a SV-wave(P-wave). The reflections of these waves are shown in Figure 2.3.

The effect that a single type of incident wave reflects as two different waves is called mode conversion. For the plane-strain case of a harmonic wave travelling in the unbounded x_1, x_2-plane, a mathematical description of the displacement field is given by

$$\mathbf{u}^{(n)} = A_n \mathbf{d}^{(n)} e^{ik_n(x_1 p_1^{(n)} + x_2 p_2^{(n)} - c_n t)}\,. \tag{2.25}$$

Here, n denotes the longitudinal- or shear-wave, k_n the previously defined wavenumber and c_n the respective wavespeed of wave n. Using these definitions, a relationship

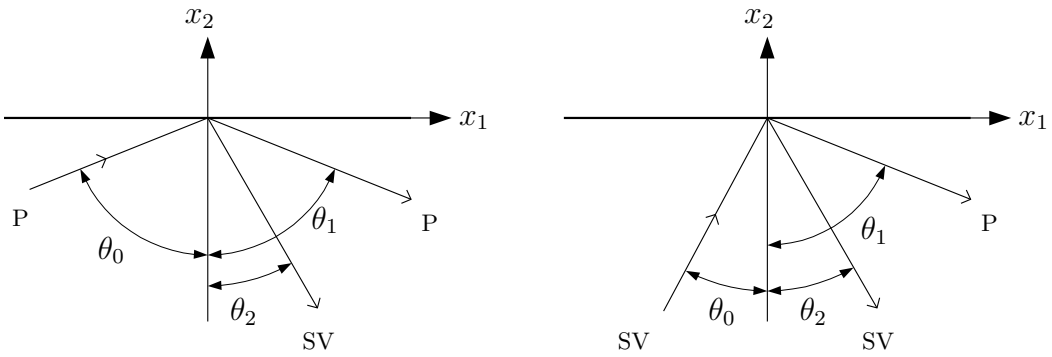

(a) Reflection of a P-Wave (b) Reflection of a SV-Wave

Figure 2.3: Wave reflections on a stress free surface

between the angle of the incident wave and the angles of the reflected ones can be determined while the circular frequency ω remains equal for the incident and the reflected waves. Table 2.1 summarizes these relationships.

Non-trivial amplitudes A_n are obtained, if the angles of incident and reflected waves, θ_0, θ_1 and θ_2 as defined in Figure 2.3, satisfy Snell's law of reflection:

$$k_0 \sin\theta_0 = k_1 \sin\theta_1 = k_2 \sin\theta_2 \,. \tag{2.26}$$

Exceptions of mode conversion are the normal incidence with $\theta_0 = 0$, which is of specific importance for the conducted research. In this case, the waves are reflected as themselves, i.e. no mode conversion occurs.

If the angle θ_0 is greater than a critical angle,

$$\theta_{\text{critical}} = \arcsin \frac{c_\text{S}}{c_\text{L}} \,, \tag{2.27}$$

then only a SV-wave is reflected. In this case, the P-wave part of the reflected signal

Table 2.1: Angle relations for reflection on a stress free surface

Incident	**Reflected P θ_1**	**Reflected SV θ_2**
P	$\theta_1 = \theta_0$	$\sin\theta_2 = (c_\text{S}/c_\text{L}) \sin\theta_0$
SV	$\sin\theta_1 = (c_\text{L}/c_\text{S}) \sin\theta_0$	$\theta_2 = \theta_0$

degenerates into a so called Rayleigh surface wave that travels along the surface with an exponentially decreasing amplitude in the negative x_2-direction.

2.3 Wave Attenuation

The most important concept of wave propagation used in this research is the phenomenon of ultrasonic attenuation. This section gives an introduction to attenuation and its mathematical representation and explains several attenuation mechanisms with their underlying physical principles.

Usually, attenuation is incorporated in the previously discussed framework by the definition of a complex wave number $\widetilde{k}$. To that purpose, Eq. 2.19 is expanded in the following fashion:

$$\widetilde{k} = \frac{\omega}{c} + i\alpha \,, \tag{2.28}$$

where α describes the wave attenuation coefficient. As will be shown later, the complex wavenumber can be used equivalently to a complex wave speed or complex material properties. Substitution of the complex wavenumber in the displacement function of a harmonic wave, Eq. 2.18, yields

$$u(x,t) = Ae^{i(\widetilde{k}x-\omega t)} = Ae^{i((\frac{\omega}{c}+i\alpha)x-\omega t)} \,, \tag{2.29a}$$

which can also be written as

$$u(x,t) = Ae^{-\alpha x}e^{i(kx-\omega t)} \;\text{ for }\; x \geq 0 \,. \tag{2.29b}$$

In the latter equation, the first part of the right hand side describes an exponential decay in amplitude, $Ae^{-\alpha x}$ in the direction of propagation while the second part describes the harmonic behavior as in Eq. 2.18.

In general, the attenuation coefficient α is a function of frequency ω. As will be seen later, this frequency-dependence can be used for material characterization.

In conclusion,

$$\alpha = \alpha(\omega) = Im\{\widetilde{k}\} \,. \tag{2.30}$$

As a measure of the decay in amplitude, consider two amplitudes A_0 and A_1 of a wave at two positions seperated by the propagation distance Δx. A relation between these two amplitudes is given by

$$A_1 = A_0 e^{-\alpha \Delta x} \,, \tag{2.31a}$$

from which the attenuation is found to be

$$\alpha = \frac{1}{\Delta x} \ln(\frac{A_0}{A_1}) \,. \tag{2.31b}$$

In order to express the attenuation coefficient in terms of the commonly used measures decibels (dB) and nepers (Np) that are described as

$$20 \log_{10}(\frac{A_0}{A_1}) \text{ [dB]} \quad \text{and} \quad \ln(\frac{A_0}{A_1}) \text{ [Np]} \,, \tag{2.32}$$

Eq. 2.31(b) has to be rewritten as

$$\hat{\alpha} = \frac{1}{\Delta x} 20 \log_{10}(\frac{A_0}{A_1}) \text{ [dB/unit length]} \,, \tag{2.33a}$$

$$\alpha = \frac{1}{\Delta x} \ln(\frac{A_0}{A_1}) \qquad \text{[Np/unit length]} \,. \tag{2.33b}$$

A relationship between these units is given by

$$\hat{\alpha} = 20 \log_{10}(e) \cdot \alpha \approx 8.686 \cdot \alpha \,. \tag{2.34}$$

The causes of ultrasonic wave attenuation are described in the following sections. In every attenuation measurement, the attenuation coefficient is a mix of each of these mechanisms. Generally, it is not possible to seperate each of these mechanisms out in order to determine each mechanism's portion of the overall attenuation. As will be seen later, this is a critical issue for material characterization since only some effects carry valuable information about the material's microstructure while other mechanisms are disturbances introduced by several physical effects of wave propagation.

2.3.1 Extrinsic Attenuation

Attenuation mechanisms that arise as a consequence of the practice of the measurement method are refered to as extrinsic attenuation effects. The most important phenomenon in this research is the diffraction effect, which is caused by beamspreading and gives rise to a decay in amplitude as the wave propagates [9].

This effect may cause large errors in attenuation measurements and has to be accounted for. Rogers and Van Buren found an analytical expression for the diffraction correction coefficient for a plane circular piston source as it is the case for a round, finite size transducer of radius b [28]. The diffraction correction can thus be calculated as

$$D(s) = 1 - e^{-i(2\pi/s)}[J_0(2\pi/s) + iJ_1(2\pi/s)]\,, \tag{2.35}$$

where s denotes the normalized propagation distance

$$s = \frac{\Lambda \Delta x}{b^2} \tag{2.36}$$

and J_0 and J_1 are Bessel functions of zeroth and first order, respectively.

2.3.2 Intrinsic Attenuation

In the following, the two basic physically interesting intrinsic attenuation effects are described.

Viscoelastic Material Behavior - Material Absorption

In the general theory of elasticity, it is assumed that an elastic material stores energy without dissipation during deformation. This holds true for a number of materials (e.g. steel, aluminum) that are only dissipative for very high ultrasonic wave frequencies. However, there are materials of technical interest (e.g. polymers, composites, cement based materials) that dissipate some of the stored energy even in a lower frequency range. These materials are called viscoelastic, because they combine the properties of an elastic solid and a viscous liquid. During deformation, some portion

of the stored energy in these materials is converted into heat due to internal friction which causes an ultrasonic wave to lose some of its energy, resulting in a decreasing amplitude. This attenuation mechanism is often referred to as material absorption. Commonly, it is assumed to have a linear dependency on frequency in the range of ultrasound frequency, and is called hysteresis absorption [29]. This behavior can be explained by considering a material damping model which is linearly dependent on the particle velocity which increases linearly with increasing frequency.

The material absorption of a specific material is usually incorporated into the theory of attenuation by applying a material absorption parameter

$$\alpha_a(\Lambda) = \frac{C_a}{\Lambda}\,, \tag{2.37}$$

where C_a is a medium constant.

Scattering Attenuation

The other important part of intrinsic attenuation is scattering. It arises in heterogeneous materials at the interfaces of phases with different acoustic properties. These interfaces can be associated with the grain structure, crystal defects or multiple phases of inclusions within the material i.e. any inhomogeneity of the material can give rise to wave scattering.

Based on the ratio of scatterer size a and wavelength Λ, different domains are distinguished that have different approximations for the frequency dependence of the attenuation coefficient [2, 10].

The Rayleigh Domain:

$$\alpha_s(a, \Lambda) \sim \frac{a^3}{\Lambda^4} \;\text{ for }\; \Lambda >> a\,, \tag{2.38}$$

The Stochastic Domain:

$$\alpha_s(a, \Lambda) \sim \frac{a}{\Lambda^2} \;\text{ for }\; \Lambda \approx a\,, \tag{2.39}$$

The Geometric Domain:

$$\alpha_s(a, \Lambda) \sim a^{-1} \text{ for } \Lambda << a \, . \tag{2.40}$$

A mathematical approach to model the effects of scattering is generally difficult to perform. Several apporaches have been made and are presented in Chapter 3.

The total extrinsic attenuation, which is of interest in this research, is found to be the addition of the previously discussed effects of material absorption and scattering. Thus, the total attenuation can be written as

$$\alpha(a, \Lambda) = \alpha_a(\Lambda) + \alpha_s(a, \Lambda) \, . \tag{2.41}$$

CHAPTER III

MODELING OF WAVE ATTENUATION

The theoretical modeling of ultrasonic attenuation in inhomogeneous media has been approached by researchers over the last decades in several ways with the goal to enable predictions of a specific attenuation behavior in different types of materials. These predictions can be used for design purposes, optimization and material characterization.

Modeling of wave attenuation due to scattering effects is of particular interest because it provides valuable information about the relation between the acoustic behavior, and the microstructure of the material under consideration. The challenge in these kinds of modeling lies in the complexity and inhomogeneity of the material, especially when multiple scattering occurs due to a high scatterer density.

In this chapter, different mathematical approaches to represent wave scattering in viscoelastic materials are described and their limitations are discussed. The models are applied to the two phase material under consideration in this research, which consists of hardened cement paste with sand inclusions. Note that for the frequencies used in this research (0.5 MHz - 6 MHz), cement paste is always considered to be homogeneus, since the length scales of the material's grain structure are below the wavelengths of the waves utilized.

3.1 Independent Scattering Model

To represent the scattering effects of randomly distributed inclusions in a homogeneous material, an independent scattering approach has shown to provide useful results for the application of modeling cavities in cement-based materials [25, 27]. The

theory is based on the fundamental work on wave obstacle interactions by Brauner and Beltzer [4] and was further developed by Biwa [3] to provide a suitable scattering model for viscoelastic matrix material behavior as found in cement-based materials. In the following, the independent model described by Ying and Truell [35] and applied to various types of materials by Kim [13] is explained and applied to cement-based materials containing elastic inclusions.

3.1.1 Mathematical Description

The theory is classified as an independent scattering model because it is not capable of representing interactions between the scatterers attendant in the considered media. As a consequence, this model provides reasonable predictions only for low volume fractions η of the scattering inclusions. Since scatterer interactions usually result in higher losses of energy of the incident wave, the calculated attenuation underestimates the actual attenuation of the particulate material with high volume fractions since no multiple scattering effects are taken into account.

The model assumes a set of randomly distributed obstacles of spherical shape with radius a embedded in a viscoelastic matrix whose material absorption is characterized by α_a. The overall attenuation α can be expressed as

$$\alpha = (1-\eta)\alpha_a + \frac{1}{2} n_s \gamma^{sca} \,, \tag{3.1}$$

which is the solution of the differential equation relating the spatial decay of the time averaged energy flow with the material absorption and the scattering effects [25, 3]. Note the similar appearance of Eq 3.1 to the general form of the overall attenuation, described in Eq. 2.41. Clearly, the portion of material absorption can be distinguished from the scattering effects.

In Eq. 3.1, n_s is the number of scatteres per unit volume which for the case of a spherical inclusion is related to the volume fraction by

$$\eta = \frac{4}{3}\pi a^3 n_s \,. \tag{3.2}$$

γ^{sca} denotes the scattering cross-section described in [35] which for incident plane waves with longitudinal wavenumber k_l, and shear wavenumber k_s is given as

$$\gamma^{sca} = 4\pi \sum_{m=0}^{\infty} \frac{1}{2m+1} \left[|A_m|^2 + m(m+1)\frac{k_l}{k_s} |B_m|^2 \right] . \tag{3.3}$$

Physically, the scattering cross-section is defined as that area which, if placed into the incident field normal to the direction of propagation, would intercept a time averaged energy flux equal to that of the total scattered field through a closed surface which contains the scattering obstacle. It thus relates the energy flux of the incident wave to that of the scattered field around the inclusion, and is therefore a measure of the scattering intensity of the scatterer in the medium. The scattering cross-section is a function of the wavelength of the incident wave as well as of the scatterer's shape. For the evaluation of γ^{sca}, the coefficients A_m and B_m need to be found that specify the wave field in the matrix material and the inclusion. These can be calculated from the constraint of continuity of stress and particle displacement at the interface of the scatterer and its surrounding media. The calculations are taken from [35] and presented in Appendix A.1.

3.1.2 Model Results

For the case of a sand scatterer in a cement paste matrix, Figure 3.1 shows the scattering cross-section γ^{sca} which is normalized to the physical obstacle cross section over the normalized frequency ka of an incident longitudinal wave. At the end of this chapter, relevant cement paste and sand properties for this and the following calculations are summarized in Table 3.1 and Table 3.2, respectively.

The beginning increase of the scattering cross-section, and thus the scattering effects for increasing frequencies, can be explained by the fact that the wavelengths of lower frequency waves are much longer than the obstacle size. As a result, the influence of the scatterer on the incident wave field is nearly negligible. As the frequency of the

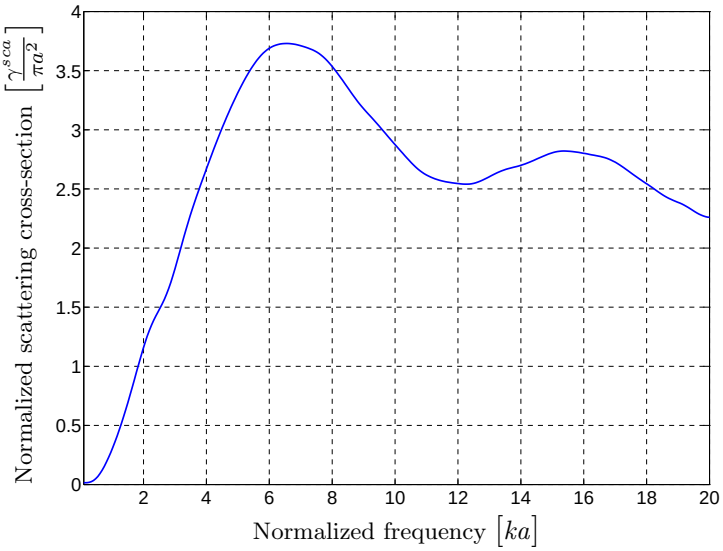

Figure 3.1: Normalized scattering cross-section for sand in cement paste

wave increases, and the decreasing wavelengths get in the range of the scatterer size, the influence of the inclusion becomes more and more relevant.

The peak with a center frequency of around $ka = 6.5$ refers to a resonance phenomenon of the scattering obstacle. The elastic inclusion of spherical shape can be considered as a vibrating system in a damped environment. As it is well known from the theory of dynamics, such systems show resonance phenomena which result in the capability of absorbing high amounts of energy in a certain frequency range. This absorption of wave energy gives rise to higher scattering effects as can be observed in the maximum values of the scattering cross section. Consequently, for the overall attenuation of the particulate material, this resonance phenomenen results in a higher attenuation coefficient.

Evaluations for the overall attenuation coefficient, Eq. 3.1, with varying volume fractions η are shown in Figure 3.2.

As would be suspected by inspection of Eq. 3.1, increasing volume fractions of the

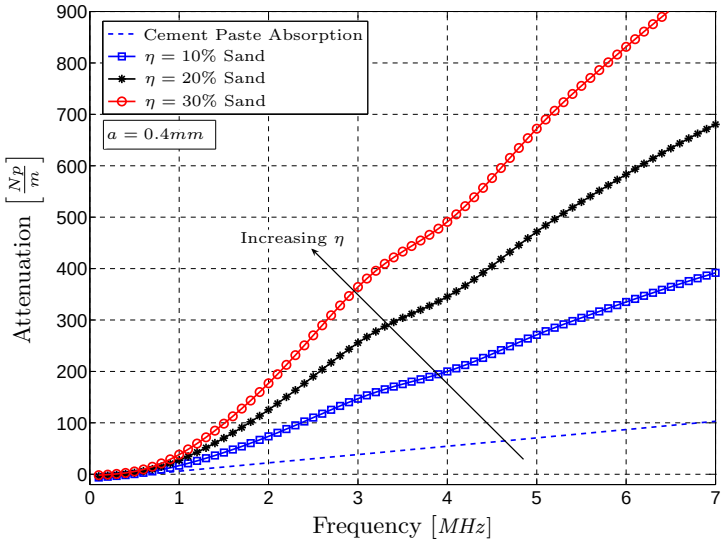

Figure 3.2: Attenuation coefficient for varying amounts of sand inclusions

included aggregate result in a linear increase in the overall attenuation for each frequency. As will be seen later, this linearity property of the independent scattering model allows for a convenient incorporation of a size distribution of the inclusions, as is found in sand and other natural aggregates.

Note that for the case of an inclusion radius of $a = 0.4\ mm$ the previously mentioned resonance phenomenon occurs at frequencies of about 10 MHz and is therefore above the frequency range considered in this research. A very small increase in attenuation, of around 3 MHz, is observed especially for higher volume fractions and may also be explained with the resonance phenomena but does not refer to the main peak that is found in the normalized scattering cross-section.

The independent scattering model presented, is a relatively easy approach to model wave scattering in particulate materials that are composed of a homogeneous matrix material with randomly distributed inclusions. For cement-based materials with air inclusions, it has shown to provide results which are in good agreement with measured wave attenuation [25].

For varying inclusion sizes within a material, the accuracy of the model predictions can be further improved by the implementation of a size distribution of the scattering obstacles as is shown for the case of air voids in [26]. Due to the linear behavior of the model and ignoring higher order scattering effects, this distribution can easily be incorporated by expanding Eq. 3.1 to

$$\alpha = (1-\eta)\alpha_a + \frac{1}{2}\sum_{i=1}^{N} n_{s,i}\ \gamma_i^{sca}\ , \tag{3.4}$$

where $n_{s,i}$ is the number of scatterers of a specific size and γ_i^{sca} denotes the scattering cross section of the respective scatterer.

The model shows its limits when the volume fraction of inclusions, and thus the number of scatterers, increase to greater than approximately 20% [18]. In this case, the assumption that no multiple scattering of the wave field occurs is no longer valid and the calculated attenuation is understated.

This fundamental limitation of the independent scattering approach is crucial for the modeling of cement-based multiphase materials which usually consist of high amounts of aggregates ($> 60\%$). For this reason, researchers have developed different modeling techniques that take multiple scattering between different inclusions into account. The basic ideas, and a specific implementation is described in the subsequent section.

3.2 Effective Medium Theory Model

The treatment of multiple wave scattering in composite materials was first developed in the Waterman and Truell theory [34] on which basis more sophisticated models evolved.

The general modeling technique used in this research is the so-called effective medium theory (EMT). This theory treats the particulate material with its acoustic behavior as a whole material, which is defined by the overall (effective) material parameters.

Therefore, the model does not directly describe the scattered waves, and its interactions within the material but describes the overall acoustic behavior on a macroscale. In the literature, many evaluations of these ideas can be found, e.g. in [11, 14]. These group of models are summarized by the term EMT and are joined by some common hypotheses.

In this research, a self-consistent model developed by Sabina and Willis [30] for homogeneous materials with randomly distributed spherical inclusions is considered and used for cement-based materials. Due to the high complexity of the model's mathematical derivation, this section describes the basic ideas of the EMT in general and provides the formulae used for the self-consistent model implemented in this research.

3.2.1 Mathematical Description

The EMT model also considers a set of randomly distributed obstacles of spherical shape in a homogeneous matrix material. For an incident plane longitudinal- or shear wave, the goal of the model is to find effective acoustic properties for the particulate material which are defined by the two elastic constants, $\tilde{\kappa}$ and $\tilde{\mu}$, as well as the effective density $\tilde{\rho}$. These complex valued properties are a function of the type and frequency ω of the incident wave field and are marked with the tilda symbol($\tilde{}$).

The basic assumption of all effective medium theory models is the self-consistency condition. The self-consistency condition states that the mean wave field in the particulate material coincides with the wave field propagating in the effective medium [11]. Furthermore, the behavior of the inhomogeneous material with N inclusions can be changed for the effective homogeneous material while each additional single inclusion $N+1$ behaves as an isolated scatterer embedded in the effective medium. With that condition, the multiple scattering problem can be simplified to the solution of a single scatterer that is embedded in a material with the effective media properties. This process of homogenization is visualized in Figure 3.3.

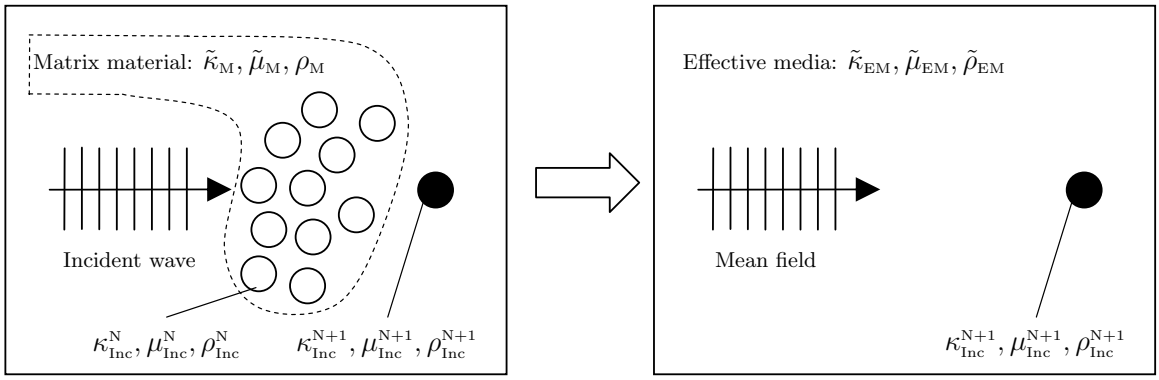

Figure 3.3: Effective medium theory approach

For the homogeneous matrix material with properties $\tilde{\kappa}_{\mathrm{M}}$, $\tilde{\mu}_{\mathrm{M}}$ and ρ_{M} that contains one type of spherical inclusions of volume fraction η and radius a with the properties κ_{Inc}, μ_{Inc} and ρ_{Inc}, following the steps of [30], the effective material properties are found to be

$$\tilde{\kappa}_{\mathrm{EM}} = \tilde{\kappa}_{\mathrm{M}} + \frac{\eta\, h(\tilde{k})h(-\tilde{k})(\kappa_{\mathrm{Inc}} - \tilde{\kappa}_{\mathrm{M}})}{1 + 3\epsilon_{\mathrm{L}} \frac{\kappa_{\mathrm{Inc}} - \tilde{\kappa}_{\mathrm{EM}}}{3\tilde{\kappa}_{\mathrm{EM}} + 4\tilde{\mu}_{\mathrm{EM}}}}\,, \tag{3.5}$$

$$\tilde{\mu}_{\mathrm{EM}} = \tilde{\mu}_{\mathrm{M}} + \frac{\eta\, h(\tilde{k})h(-\tilde{k})(\mu_{\mathrm{Inc}} - \tilde{\mu}_{\mathrm{M}})}{1 + 2(\mu_{\mathrm{Inc}} - \tilde{\mu}_{\mathrm{EM}}) \frac{2\epsilon_{\mathrm{L}}\tilde{\mu}_{\mathrm{EM}} + \epsilon_{\mathrm{S}}(3\tilde{\kappa}_{\mathrm{EM}} + 4\tilde{\mu}_{\mathrm{EM}})}{5\tilde{\mu}_{\mathrm{EM}}(3\tilde{\kappa}_{\mathrm{EM}} + 4\tilde{\mu}_{\mathrm{EM}})}}\,, \tag{3.6}$$

$$\tilde{\rho}_{\mathrm{EM}} = \rho_{\mathrm{M}} + \frac{\eta\, h(\tilde{k})h(-\tilde{k})(\rho_{\mathrm{Inc}} - \rho_{\mathrm{M}})}{1 + (\rho_{\mathrm{Inc}} - \rho_{\mathrm{EM}}) \frac{3 - \epsilon_{\mathrm{L}} - 2\epsilon_{\mathrm{S}}}{3\tilde{\rho}_{\mathrm{EM}}}}\,. \tag{3.7}$$

For an attenuative matrix material, the elastic constants $\tilde{\kappa}_{\mathrm{M}}$, $\tilde{\mu}_{\mathrm{M}}$ are functions of the frequency of the incident wave with complex wavenumber $\tilde{k}$ and are therefore complex, too. This is not the case for the density ρ_{M}, as long as the viscoelastic material is considered to be homogeneous. In the case of the cement-based materials studied in this research, the inclusions are elastic in their behavior which can be seen by the real valued material constants κ_{Inc}, μ_{Inc} and ρ_{Inc}.

For a spherically shaped inclusion, the formfunction $h(\tilde{k})$ is defined as

$$h(\tilde{k}) = 3\frac{\sin(\tilde{k}a) - \tilde{k}a\cos(\tilde{k}a)}{(\tilde{k}a)^3}\,. \tag{3.8}$$

The two parameters ϵ_{L} and ϵ_{S} are found to be

$$\epsilon_{\mathrm{L}} = \frac{3(1 - i\tilde{k}_{\mathrm{EM,L}}a)}{(\tilde{k}_{\mathrm{EM,L}}a)^3} \left[\sin(\tilde{k}_{\mathrm{EM,L}}a) - \tilde{k}_{\mathrm{EM,L}}a\cos(\tilde{k}_{\mathrm{EM,L}}a)\right] e^{i\tilde{k}_{\mathrm{EM,L}}a} , \tag{3.9}$$

and

$$\epsilon_{\mathrm{S}} = \frac{3(1 - i\tilde{k}_{\mathrm{EM,S}}a)}{(\tilde{k}_{\mathrm{EM,S}}a)^3} \left[\sin(\tilde{k}_{\mathrm{EM,S}}a) - \tilde{k}_{\mathrm{EM,S}}a\cos(\tilde{k}_{\mathrm{EM,S}}a)\right] e^{i\tilde{k}_{\mathrm{EM,S}}a} . \tag{3.10}$$

In Eq. 3.9 and 3.10, $\tilde{k}_{\mathrm{EM,L}}$ and $\tilde{k}_{\mathrm{EM,S}}$ denote the complex wavenumbers of a longitudinal and a shear wave in the effective medium, respectively. They are functions of the effective medium properties that are to be found and are defined as

$$\tilde{k}_{\mathrm{EM,L}} = \frac{\omega}{\tilde{c}_{\mathrm{EM,L}}} , \tag{3.11}$$

and

$$\tilde{k}_{\mathrm{EM,S}} = \frac{\omega}{\tilde{c}_{\mathrm{EM,S}}} , \tag{3.12}$$

with the complex phase velocities

$$\tilde{c}_{\mathrm{EM,L}} = \sqrt{\frac{\tilde{\kappa}_{\mathrm{EM}} + \frac{4}{3}\tilde{\mu}_{\mathrm{EM}}}{\tilde{\rho}_{\mathrm{EM}}}} , \tag{3.13}$$

and

$$\tilde{c}_{\mathrm{EM,S}} = \sqrt{\frac{\tilde{\mu}_{\mathrm{EM}}}{\tilde{\rho}_{\mathrm{EM}}}} . \tag{3.14}$$

Evaluation of Eqs. 3.5 - 3.7 yields the parameters $\tilde{\kappa}_{\mathrm{EM}}$, $\tilde{\mu}_{\mathrm{EM}}$ and $\tilde{\rho}_{\mathrm{EM}}$ that define the effective media. For the frequency dependent attenuation coefficient α, the complex wavenumbers, Eqs. 3.11 and 3.12, and the complex phase velocites, Eqs. 3.13 and 3.14, are used to find

$$\alpha_{\mathrm{L}} = Im\left\{\tilde{k}_{\mathrm{EM,L}}\right\} , \tag{3.15}$$

and

$$\alpha_{\mathrm{S}} = Im\left\{\tilde{k}_{\mathrm{EM,S}}\right\} , \tag{3.16}$$

for the longitudinal and shear attenuation, respectively.

3.2.2 Model Results

Eqs. 3.5 - 3.7 denote a set of coupled nonlinear algebraic equations to find the effective media properties. In the following, these equations are solved numerically using a Gauss-Newton approximation method [17]. As before, the calculated attenuation refers to a longitudinal wave in a cement paste matrix with sand inclusions whose shape is assumed to be spherical.

In order to assess the complex valued elastic constants of cement paste from the known phase velocities and attenuation coefficients, the formulae for the complex wavenumber and phase velocity, Eqs. 3.11 - 3.14, are used again.

$$\tilde{c}_{\mathrm{M,L}} = \frac{\omega}{\tilde{k}_{\mathrm{M,L}}} = \frac{\omega}{\frac{\omega}{c_{\mathrm{L}}} + i\alpha_{\mathrm{M,L}}} \,, \tag{3.17}$$

and

$$\tilde{c}_{\mathrm{M,S}} = \frac{\omega}{\tilde{k}_{\mathrm{M,S}}} = \frac{\omega}{\frac{\omega}{c_{\mathrm{L}}} + i\alpha_{\mathrm{M,S}}} \,. \tag{3.18}$$

As stated before, the density ρ_{M} of the cement paste is real valued which relates to the assumption of a homogeneous material. Rearranging Eqs. 3.13 and 3.14 yields expressions for the elastic constants of the attenuative matrix material.

$$\tilde{\mu}_{\mathrm{M}} = (\tilde{c}_{\mathrm{M,S}})^2 \rho_{\mathrm{M}} \,, \tag{3.19}$$

and

$$\tilde{\kappa}_{\mathrm{M}} = (\tilde{c}_{\mathrm{M,L}})^2 \rho_{\mathrm{M}} - \frac{4}{3}\tilde{\mu}_{\mathrm{M}} \,. \tag{3.20}$$

Figure 3.4 shows the attenuation coefficient of the EMT model for different amounts of sand inclusions with a nominal radius of $a = 0.4mm$.

Besides the general increase of the attenuation coefficient for increasing frequencies of the incident wave, the model shows a peak around 3 *MHz*. While the former behavior can be explained with the hysteresis absorption of the cement paste matrix, the latter refers again to the resonance phenomenon of the scattering inclusions.

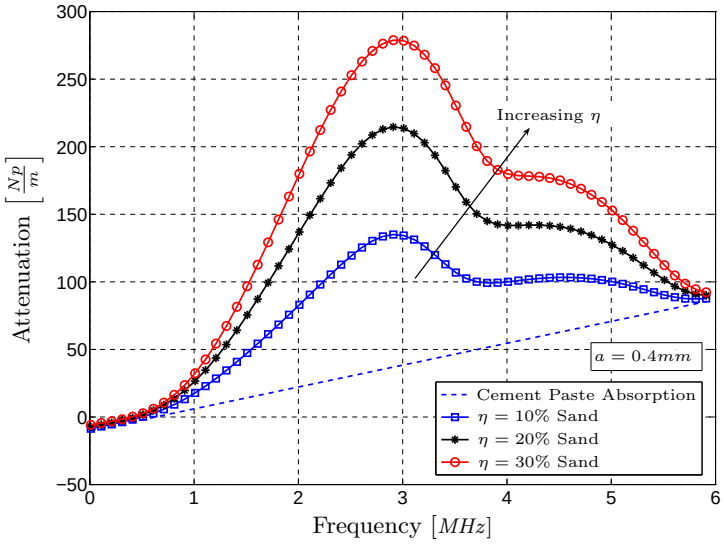

Figure 3.4: Attenuation coefficient for varying amounts of sand inclusions

The sensitivity of the EMT model to the input parameter η is also illustrated in Figure 3.4. As is the case for the independent scattering model, the attenuation coefficient increases for higher volume fractions of inclusions. However, in the case of the EMT model, the linearity of that property does not hold true any more due to the involvement of multiple scattering effects.

In order to implement a size distribution of the scattering inclusions, the non-linear terms of the EMT model, Eqs. 3.5 - 3.7, have to be expanded. While this expansion is still feasible, it is no longer as convenient as in the independent scattering model, especially when a large number of different scatterer sizes are involved.

While the EMT approach has fundamental advantages over the independent scattering model to quantify attenuation in particulate materials, some limitations of the EMT model are important.

Due to the assumption of a constant stress field in the inclusion, the presented model is only valid up to frequencies in the range of the first resonance frequency, see [12].

In the literature, very few works for the short wavelength range are available. Kanaun et al. [11] provide a sophisticated model based on the EMT approach that is supposed to cover the whole frequency range.

Note that at the present time, self-consistent EMT approaches remain the only efficient solutions for the many particle problem of wave propagation in particulate composites with contrast properties of the multiple phases.

Table 3.1: Material properties for cement paste

Property	**Symbol [Unit]**	**Value**
Longitudinal wavespeed	$c_{\mathrm{L}}\left[\frac{m}{s}\right]$	3680[1]
Shear wavespeed	$c_{\mathrm{S}}\left[\frac{m}{s}\right]$	1990[2]
Density	$\rho\left[\frac{Kg}{m^3}\right]$	1970[1]
Longitudinal attenuation	$\alpha_{L0}\left[\frac{Np}{m}\right]$	-10.19[1]
$\alpha_L(f) = \alpha_{L0} + \alpha_{La} f$	$\alpha_{La}\left[\frac{Np}{m \cdot MHz}\right]$	16.18[1]
Shear attenuation	$\alpha_{S0}\left[\frac{Np}{m}\right]$	8.85[2]
$\alpha_S(f) = \alpha_{S0} + \alpha_{Sa} f$	$\alpha_{Sa}\left[\frac{Np}{m \cdot MHz}\right]$	90.46[2]

Table 3.2: Material properties for quartz sand [21]

Property	**Symbol [Unit]**	**Value**
Longitudinal wavespeed	$c_{\mathrm{L}}\left[\frac{m}{s}\right]$	5570
Shear wavespeed	$c_{\mathrm{S}}\left[\frac{m}{s}\right]$	3540
Density	$\rho\left[\frac{Kg}{m^3}\right]$	2600
Bulk modulus	$\kappa\ [GPa]$	36.96
Shear modulus	$\mu\ [GPa]$	32.58

[1] Measured values, Chapter 5

[2] Values taken from Punurai et al. [25]

CHAPTER IV

EXPERIMENTAL PROCEDURE

For the characterization of the properties of cement-based materials using ultrasonic wave attenuation, it is crucial to have a reliable and repeatable measurement technique. Over the years, several types of measurements for different applications have been developed [2, 23, 32].

The challenge in measuring attenuation of particulate materials lies in their inhomogeneous microstructure and in their relatively highly attenuative nature. Furthermore, the contact measurement technique used in this research tends to be very sensitive to external influences, especially the coupling conditions between the measurement transducers and the specimen. Due to the high amount of wave energy required to perform attenuation measurements on highly attenuative materials, contact measurement techniques are often preferred. Moreover, the widely used immersion technique, where the coupling problem is solved by immersing the whole measurement setup into a water bath, cannot be utilized in the case of cement-based materials since the surrounding water would be soaked into the specimen where it would significantly change the material's attenuation behavior, that is to be determined.

To provide reasonable attenuation measurements for cement-based particulate materials, this research develops a measurement technique following a six step sequence based on two general types of attenuation measurements. The sequence incorporates reflection coefficient measurements as a quantitative measure of the coupling and clamping conditions between the specimen and the measuring transducers. It is shown that for certain specimen-transducer pairings, the assumption of a free surface

reflection as it was used by former researchers is not valid since the transducers have a significant influence on the reflection behavior. Consequently, the proposed sequence shows the capability to produce repeatable results with a significant reduction in the amount of uncertainty compared to existing contact measurement techniques.

The following chapter describes the experimental setup and the specimens used in this research. The two basic attenuation measurement techniques are explained and their signal processing procedure is provided. The importance of the reflection coefficient of the transducer interface is pointed out and the developed six step method is explained. A reference measurement of a relatively simple material shows the robustness of the proposed measurement technique.

4.1 General Measurement Methods

As described in Section 2.3, the attenuation coefficient α describes the exponential decrease in amplitude of a propagating plane wave. In order to assess this coefficient, attenuation measurement techniques basically compare the amplitudes of the travelling wave at different propagation distances.

In this research, two types of measurement techniques are used that differ in the number of transducers that are involved and in the respective propagation distances of the two signals that are compared for the evaluation of the attenuation coefficient.

4.1.1 Through Transmission Attenuation Measurements

The first measurement technique is called through transmission measurement because it involves two transducers on each surface of the specimen whereas the wave is launched on one side and detected on the other side. The general setup of the measurement is shown in Figure 4.1.

To launch an ultrasonic wave into the material, a pulse generator (Panametrics Inc., 5072 PR) is used to generate an electric impulse of up to 360 V and a bandwidth of

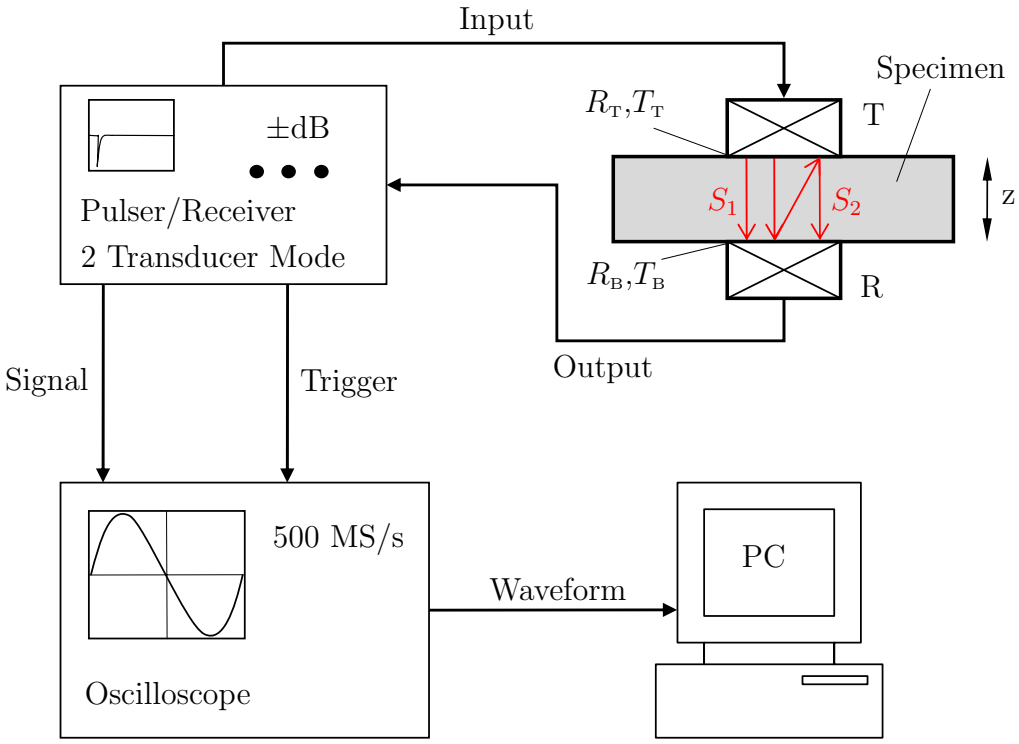

Figure 4.1: Through transmission measurement setup

up to 35 *MHz*. The electric impulse excites an incident broadband transducer (T) of 2.25 *MHz* and 5 *MHz* nominal frequency and a radius of $b = 6.35mm$ (Panametrics Inc.) that converts it into a pressure wave that propagates through the specimen. Notice that in this research only longitudinal waves are used for material characterization. Regarding the bandwidth of both types of broadband transducers, the frequency range between 0.5 *MHz* and 7 *MHz* can be securely covered with a sufficient amount of incident wave energy.

The arriving wave is detected by the receiving transducer (R) and is converted into an electric signal using the same type of broadband transducers as for the incident wave. The electric signal is amplified with a maximum gain of 50 *dB* by the integrated amplifier of the pulse generator. The amplified signal is acquired by a digital oscilloscope with a sampling frequency of 500 MS/s and a signal length of $30,000$ points ($\hat{=}$ 60 μs). By averaging over a large number of waveforms (i.e. $n = 512$), the signal to noise ratio (SNR) is significantly increased. The oscilloscope is triggered

by a rectangularly shaped trigger signal generated by the pulse generator. For the subsequent signal analysis, the data is transferred to a computer and processed with the software package matlab.

To ensure an on axis alignment of both transducers, a mechanical fixture is utilized that clamps the transducers in a defined position with a fixed pressure throughout the measurement. The fixture also enables the clamping and unclamping of each of the transducers independently while the specimen still remains in its position and no disturbance is introduced to the coupling conditions between the transducer and the specimen. A light coupling oil is used to assure sufficient contact between the specimen surface and the transducers.

The most important assumptions of all measurements and signal processing used in this research are the assumption of a linear, time-invariant behavior of the whole system and the reciprocal behavior of the transducers used. The latter describes the fact that the transducers show the same transfer function whether they are used in the transmitting or receiving mode.

In the described measurement setup, two signals are considered. The first signal travels through one specimen thickness z and is denoted with S_1, while the second signal S_2 reflects on both sides of the specimen and therefore has a propagation distance of $3z$, as shown in Figure 4.1. These two signals are windowed out of the acquired time domain signal using a rectangular window and are transformed into the frequency domain employing a fast Fourier transformation (FFT) algorithm [22]. To assess the attenuation coefficient in the frequency band covered by the transducer, a spectral analysis technique proposed by Sears et al. [31] is utilized. The spectra of the two signals can be expressed as

$$S_1(f) = IT_{\mathrm{T}}T_{\mathrm{B}}D(z)e^{-\alpha z}e^{i[kz-\omega t+\phi_0]}\,, \tag{4.1}$$

and

$$S_2(f) = IT_{\mathrm{T}}R_{\mathrm{B}}R_{\mathrm{T}}T_{\mathrm{B}}D(3z)e^{-\alpha 3z}e^{i[k3z-\omega t+\phi_0]}\,, \tag{4.2}$$

where $I(f)$ denotes the spectrum of the incident signal, T_{T}, T_{B}, R_{T} and R_{B} are the respective transmission and reflection coefficients of the top and bottom interfaces between the specimen and the transducer. Since the functions of the incident and receiving transducers are interchanged later in this research, the interfaces are denoted with 'Top' and 'Bottom' rather than 'Transmitting' and 'Receiving'. ϕ_0 expresses the phase offset of the incident signal, while $D(z)$ and $D(3z)$ are the diffraction coefficients described by Rogers and Van Buren [28] and in Section 2.3 for the respective propagation distances of z and $3z$. To evaluate these coefficients, the frequency dependent phase velocity c of the dispersive media has to be found. Combination of Eq. 4.1 and Eq. 4.2 yields

$$\left|arg(\frac{S_1}{S_2})\right| = |kz-\omega t+\phi_0-(k3z-\omega t+\phi_0)| = 2kz = \frac{4\pi fz}{c}\,, \tag{4.3a}$$

or

$$c(f) = \frac{4\pi fz}{\left|arg(\frac{S_1}{S_2})\right|}\,, \tag{4.3b}$$

where $|arg(\cdot)|$ denotes the magnitude of the unwrapped phase of the complex number, i.e. corrected by the 2π equivalent jumps.

After the evaluation of $D(z)$ and $D(3z)$, using the spectral ratio technique, the expression for the attenuation coefficient is found to be

$$\frac{|S_1|}{|S_2|} = \frac{IT_{\mathrm{T}}T_{\mathrm{B}}D(z)e^{-\alpha z}}{IT_{\mathrm{T}}R_{\mathrm{B}}R_{\mathrm{T}}T_{\mathrm{B}}D(3z)e^{-\alpha 3z}} = \frac{1}{R_{\mathrm{B}}R_{\mathrm{T}}}\frac{D(z)}{D(3z)}e^{\alpha 2z}\,, \tag{4.4a}$$

or

$$\alpha(f) = \frac{1}{2z}\left[\ln\left(\frac{|S_1|}{|S_2|}\right) - \ln\left(\frac{D(z)}{D(3z)}\right) + \ln(R_{\mathrm{B}}R_{\mathrm{T}})\right]\,. \tag{4.4b}$$

The sequence of signal processing and the respective results are summarized in Figure 4.2. A typical time domain signal and the windowed signals of interest S_1 and

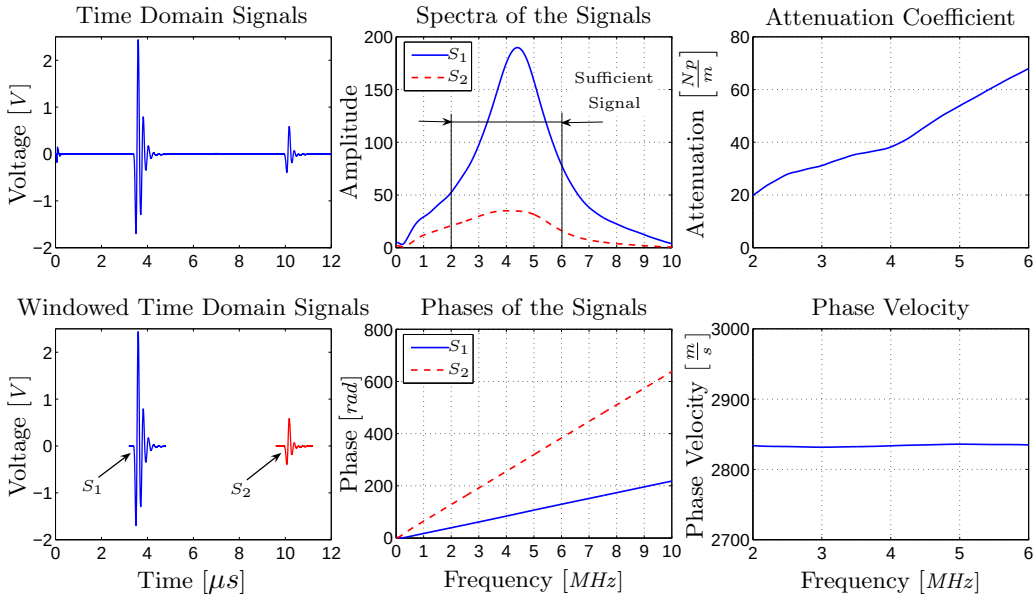

Figure 4.2: Signal processing

S_2 are shown. The spectra of the two signals give information about the wave's amplitude of the respective frequency, and are therefore an indicator of the bandwidth of the two signals. By inspection of these bandwidths, the frequency range in which the evaluated results for the phase velocity and attenuation will be reliable can be estimated. For frequencies with a very low wave amplitude, the SNR is too low to interpret the data in a reliable fashion. Note that the bandwith for reliable results might be considerably smaller than the bandwith of the transducers, depending on the level of attenuation for the respective material and frequency range.

Figure 4.2 also shows the unwrapped phases of the two signals over the frequency range which are only of interest for the calculation of the phase velocity. It is observed that the phase of S_2 is always higher than the phase of S_1 which can be explained by the longer propagation distance.

The resulting phase velocities and the attenuation coefficients as functions of frequency are also shown in Figure 4.2.

Through transmission attenuation measurements are a relatively fast and easy way

to determine a material's attenuation coefficient over a broad frequency range. Since the maximum travel distance of the signals to be compared to each other is only $3z$, through transmission measurements are a sophisticated and reliable measurement technique, especially for media with high attenuation. Besides that, their advantage lies in the fact that two signals are compared to each other that have the exact same input signal. In practice, this property is of specific importance since the amplitude of an incident wave of a certain frequency depends on the transducer's characteristics and on the coupling situation between the transducers and the specimen. Specifically, the latter issue might result in large deviations in conducted measurements. The described method defines an effective approach to avoid the comparison of signals with different coupling conditions. In Section 4.2, a method of incorporating the effect of the boundary layer by integrating the reflection coefficients is presented that results in even more repeatable and reliable results. The knowledge of these reflection coefficients for both transducers in their specific coupling situation is necessary for through transmission measurements and has to be evaluated for each single measurement setup. To solve that problem, Section 4.4 presents a combined measurement sequence.

Nevertheless, through transmission measurements, as most of other attenuation measurements, have limitations for highly attenuative media. Since the amplitude of the wave under consideration decreases dramatically in these materials, the SNR of the second signal is often too low to be able to interpret the results in a reliable fashion.

4.1.2 Double Echo Measurements

A similar method for attenuation and dispersion measurements are double echo measurements. They mainly differ in the number of transducers that are involved and therefore in the type of signals and their propagation distances that are compared to each other.

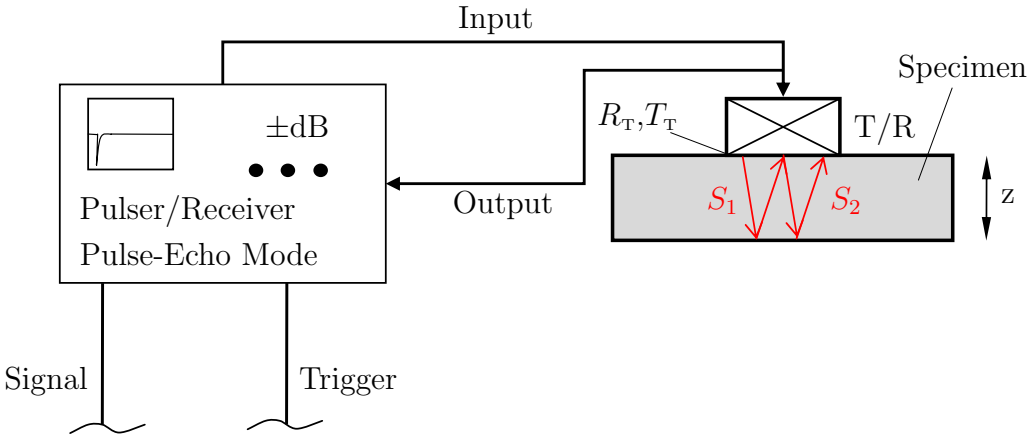

Figure 4.3: Double echo measurement scheme

Double echo attenuation measurements only use one broadband transducer that acts as the transmitting and receiving transducer at the same time. The transducer again, is excited by a short electrical impulse that is converted into a pressure wave. After the signal is reflected at the free surface of the specimen for the first time, the same transducer detects the reflected signal (echo) and transforms it into an electrical signal that is amplified by the amplifier and transferred to the oscilloscpe. The same procedure is done for the second reflection. The two captured signals again are denoted with S_1 and S_2, see Figure 4.3.

The signal processing of the obtained signals is very comparable to the through transmission technique. The only differences in the spectral ratio analysis are the propagation distances of $2z$ and $4z$ for the signals S_1 and S_2, respectively. Analogous to the through transmission measurements, the frequency domain represantations of the signals are

$$S_1(f) = I(T_T)^2(-1)D(2z)e^{-\alpha 2z}e^{i[k2z-\omega t+\phi_0]}\,, \tag{4.5}$$

and

$$S_2(f) = I(T_T)^2(-1)^2R_T D(4z)e^{-\alpha 4z}e^{i[k4z-\omega t+\phi_0]}\,, \tag{4.6}$$

while the reflection coefficient of the free surface is assumed to be $R_B = -1$. From

that, the phase velocity and the attenuation coefficient again are found to be

$$c(f) = \frac{4\pi f z}{\left| arg(\frac{S_1}{S_2}) \right|} , \tag{4.7}$$

and

$$\alpha(f) = \frac{1}{2z} \left[\ln\left(\frac{|S_1|}{|S_2|}\right) - \ln\left(\frac{D(2z)}{D(4z)}\right) + \ln(R_{\mathrm{T}}) \right] . \tag{4.8}$$

In comparison with through transmission attenuation measurement setups, double echo methods have the significant advantage that only one transducer is used to perform the measurement. Thus, they enable the inspection of materials that are only accessible from one side or where other circumstances prevent the use of two transducers, see Pezant et al. [24]. Moreover, double echo methods only require the knowledge of one reflection coefficient and therefore reduce the amount of uncertainty that goes along with the problem of repeatable coupling conditions.

However, the maximum propagation distance of the considered signals is $4z$ in comparison to $3z$ as in the case of through transmission measurements. This limits the application of double echo measurements for either highly attenuative or very thick samples because the amplitude and hence the SNR of the second signal becomes too small to interpret the obtained results in a reliable fashion. In practice, a low SNR results in the inability to define a clear starting and ending point of the second signal which is necessary for the signal processing sequence.

4.2 Reflection Coefficient Analysis

As previously mentioned, the reflection coefficient is a quantitative measure of the interactions that occur at the interface of different materials. Specifically, it describes the decrease in amplitude and the phase change when a wave is reflected at a certain interface.

This section describes the theory of the reflection coefficient between the specimens

and the transducers as it is used in this research. Furthermore, it provides a measurement technique to determine the reflection coefficient of a specific interface. A transducer related resonance phenomenon that occurs in the material pairing used in this research is explained before the influence of the reflection coefficient analysis for attenuation measurements is shown. A more detailed explanation of reflection coefficients in general is given in [6].

In general, the reflection coefficient is a function of the wave's frequency. Moreover, it depends on several other factors that can change its magnitude and therefore the conducted attenuation measurements in a significant fashion. Zhang et al. [36] describe the influence of the couplant layer thickness as it is present between the transducer and the specimen surface. The effect of the clamping pressure on the transducer is investigated by Lavrentyev and Rokhlin [16]. It is stated that the assumption of a perfect interface does not hold true any more when a pressure is applied on the interface.

Since the reflection coefficient of a specific specimen-transducer interface is sensitive to outer influences of the measurement setup, it is almost impossible to reproducibly attach the transducers to the specimen for each measurement setup that is conducted. Therefore, the only suitable method to obtain repeatable results is to always measure the reflection coefficients for each of the specific setups in which an attenuation measurement is carried out.

4.2.1 Reflection Coefficient Measurements

Generally, the reflection coefficient for a specific material interface can be calculated using Eq. 2.23. However, it requires the knowledge of the dispersion relationship and the exact material properties for the considered interface, – it is difficult to obtain the former. For that reason, a more practical approach is to directly measure the

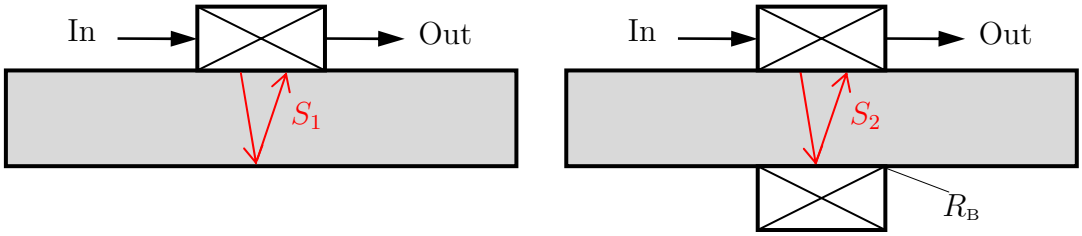

(a) Free surface (b) Mounted transducer

Figure 4.4: Reflection coefficient measurement setup

reflection coefficient of interest.

In this research, a simple method is used to determine the reflection coefficient of a transducer-specimen interface under the current coupling and clamping conditions. The method again uses a spectral ratio analysis technique which is based on a pulse-echo measurement in a one transducer setup. The two signals to be compared to each other are the first echo of a reflected signal of a free surface (S_1) and the first echo of a reflected signal of the clamped transducer surface under consideration (S_2), compare Figure 4.4.

Assuming the reflection coefficient of the free surface as $|R_{Free}| = 1$, using the spectral ratio analysis technique,

$$\frac{|S_2|}{|S_1|} = \frac{I(T_T)^2 D(2z) e^{-\alpha 2z} R_B}{I(T_T)^2 D(2z) e^{-\alpha 2z}(1)}\,, \tag{4.9a}$$

the reflection coefficient is found to be

$$R_B = \frac{|S_2|}{|S_1|}\,. \tag{4.9b}$$

The spectra of two representative signals S_1 and S_2 and the resulting reflection coefficient for a 5 MHz transducer are shown in Figure 4.5.

4.2.2 Transducer Resonance Phenomenon

Figure 4.5(b) shows a significant drop in the reflection coefficient around 4.1 MHz which seems to coincide with the peak value of the incident transducer's frequency

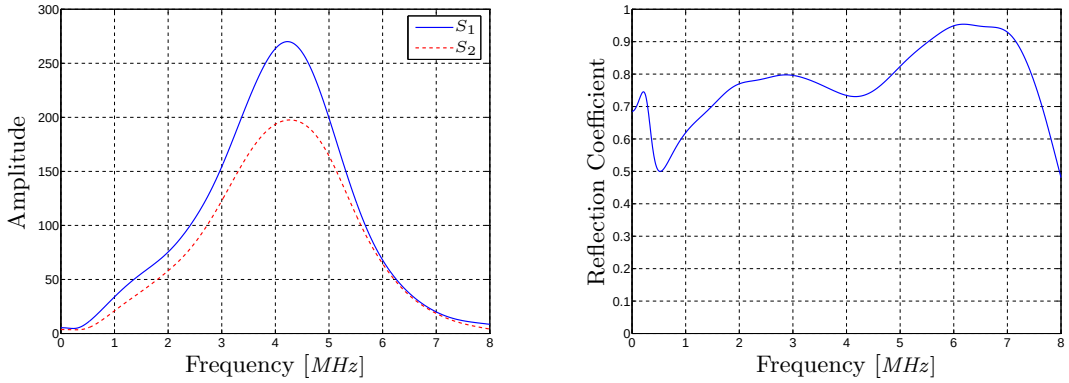

(a) Spectra of the signals

(b) Reflection coefficient

Figure 4.5: Reflection coefficient analysis: Signals and result

spectrum, see Figure 4.5(a). The drop in the reflection coefficient can be explained as a resonance phenomenon of the lower transducer whose reflection coefficient is measured in the described setup. Note that even though the depicted frequency spectrum of the signal S_1 belongs to the upper rather than to the lower transducer, it can be assumed that both characteristics look similar since the transducers are of the same type.

The center of the spectrum of a broadband transducer is an indicator of its resonance frequency while in this range a high amount of wave energy is generated. Conversely, in the range of the drop, the resonance frequency of the lower transducer is excited which gives rise to a high absorption of wave energy. Hence, the amplitude of the reflected wave is lower, which is quantitatively described by the lower reflection coefficient in this frequency range.

In order to demonstrate this behavior, the following experiment is conducted. The reflection coefficients of two transducers with different center frequencies are evaluated using the same free surface signal. As in all of the reflection coefficient measurements, the lower transducer does not have an electrical function in this setup. The transducers used in the experiment have a nominal center frequency of 5 *MHz* (same type as the incident transducer) and 2.25 *MHz* and are the two only types used in

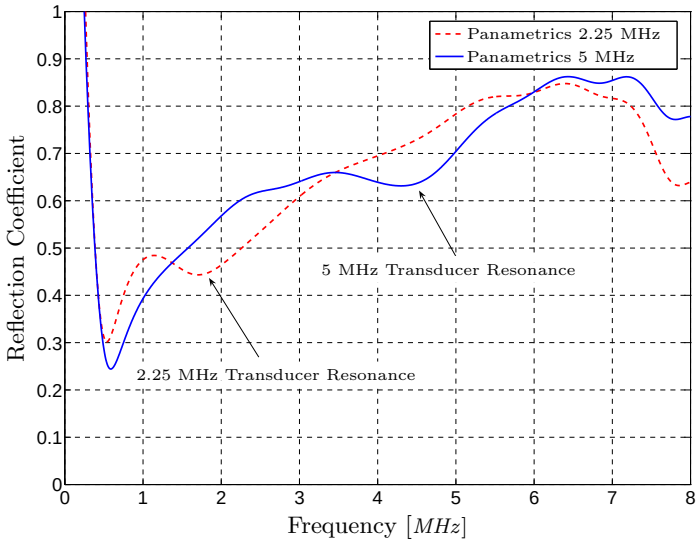

Figure 4.6: Resonance phenomenon in the reflection coefficient

this research. The behavior is shown for a cement paste specimen which is of specific interest in the conducted research. The results are shown in Figure 4.6. Clearly, the drop coincides with the center frequency of the transducer whose reflection coefficient is evaluated, i.e. the 2.25 *MHz* transducer has a drop around 1.9 *MHz* while the 5 *MHz* transducer shows the drop around 4.3 *MHz*. The general increase of the reflection coefficient for increasing frequencies is in accordance with the behavior described in [36].

Even though the conducted experiment gives a hint in order to explain the drop, a full combined electroacoustic analysis is needed to prove this observation.

4.2.3 Influence of Reflection Coefficient in Attenuation Measurements

For through transmission and double echo attenuation measurements, the influence of the reflection coefficient is crucial. However, in the literature, very little attention is paid to this fact, and there are no published results that describe a measurement technique that takes the reflection coefficients for the transmitting and receiving transducers into account. As will be shown in this section, ignoring their influence, and by

that implicitely assuming free surface reflections with no decrease in amplitude, leads to two basic problems which are the overestimation of the attenuation coefficient and a higher deviation and uncertainty throughout each measurement set.

Regarding the first problem, if the reflection coefficients are not taken into account properly, the measured attenuation coefficient is overestimated since all the decrease in wave amplitude is refered to the material attenuation rather than precisely divided into material attenuation and reflection effects. For all of the transducer-specimen pairings investigated in this research, using the proposed clamping and coupling conditions, the magnitude of the reflection coefficient is always below 1, i.e. the real reflection conditions cannot be modeled with the assumption of a free surface.
The resulting overestimation of the attenuation coefficient can easily be identified by inspection of the attenuation coefficient's mathematical definition, Eq. 4.4(b) and Eq. 4.8 for a through transmission and a double echo method, respectively. Considering the last sum term of each expression, for $|R_{\mathrm{T}}|, |R_{\mathrm{B}}| < 1$, it always holds true that $\ln(R_{\mathrm{B}}R_{\mathrm{T}}) < 0$ or $\ln(R_{\mathrm{T}}) < 0$ for the respective case of a through and a double echo measurement. Consequently, the term is negative which leads to a lower attenuation coefficient in both cases. By taking reflection effects into account, this lower coefficient describes the true material attenuation.

Considering the second problem, measuring the reflection coefficients also provides a quantitative description of the coupling and clamping conditions of a specific transducer-sample setup. Still, the problem of producing repeatable conditions remains challenging but the incorporation of a quantitative measure of the coupling and clamping conditions substantially diminishes the amount of uncertainty and reduces the variance among different measurement setups.

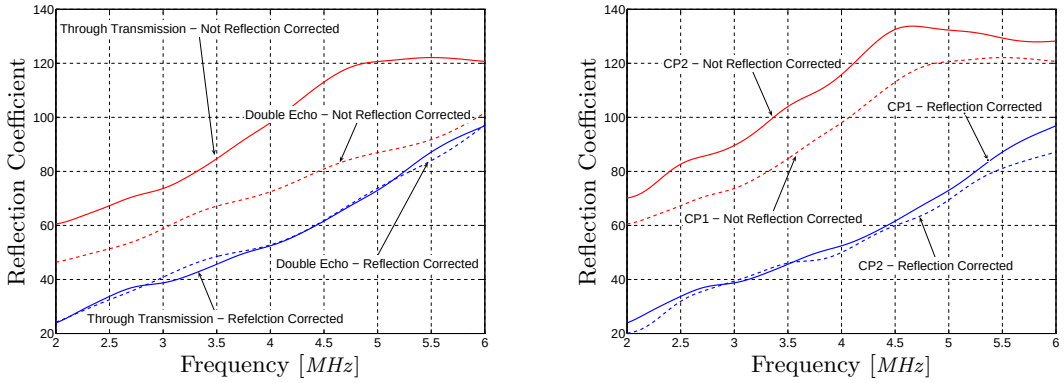

(a) Same sample (b) Different samples

Figure 4.7: Influence of the reflection coefficient

Both effects of the incorporation of the reflection coefficient are shown in Figure 4.7. Figure 4.7(a) compares two attenuation measurements of the same specimen (Cement paste I) and at the same position that only differ in their measurement setup (through transmission and double echo method).

As stated above, the consideration of the reflection coefficient results in lower values for the material attenuation. This effect is stronger in the case of the through transmission measurement, because it involves two reflection coefficients rather than just one leading to a higher overestimation of the attenuation when they are not accounted for. Furthermore, it can be seen that the attenuation curves for the through transmission and the double echo method that include reflection coefficients are very close to each other. Theoretically, these two curves should be exactly the same. Regarding the typical measurement errors present, the curves are in good agreement. On the other hand, both measurement results are shown with no reflection coefficient corrections. Clearly, the high amount of variation can be observed by the lack of agreement between the two curves. Note that the difference in the two upper curves is only due to the lack of incorporating the reflection coefficient into the analysis. Both measurements were carried out on the exact same specimen position while the transducer used for the double echo measurement remained under the same coupling

conditions for both types of measurements.

Figure 4.7(b) indicates both effects for two through transmission measurements conducted on two different specimens (Cement paste I and Cement paste II). It shows again the higher attenuation coefficient when reflection effects are not taken into account. The values of the respective curves for the two specimens differ up to about $50\frac{Np}{m}$ ($\approx$250%) for the low frequency range. The difference between the uncorrected curves can be explained by the different coupling and clamping conditions that are present in the two measurements. By incorporating the reflection effects, this repeatability cannot be completely achieved, but a measure of the current coupling and clamping conditions leads to a smaller variation, as it can be seen in the high degree of agreement for the two reflection corrected curves. Note that these curves refer to two different specimens and therefore are not even theoretically identical due to some inhomogeneity and variation among the specimens.

4.3 Diffraction Coefficient Analysis

Besides the previously described effects of the reflection coefficient, diffraction effects play another important role in the analysis of the recorded measurement data. As in the case of the reflection coefficients, the calculated attenuation is overestimated, if diffraction effects are not properly accounted for. This section briefly describes the influence of the diffraction coefficients and compares them to the reflection analysis for the case of a through transmission measurement. Note that the provided arguments can be applied to double echo meauserments in an analogous way.

4.3.1 Influence of Diffraction Correction in Attenuation Measurements

Beamspreading effects give rise to a decrease in amplitude as the waves travel in the media [9]. In general, waves radiated into the material from a finite-size source (piston) form a complex interference pattern in the mean field producing an amplitude fluctuation along the axis of radiation and tend to spread out causing amplitude decay

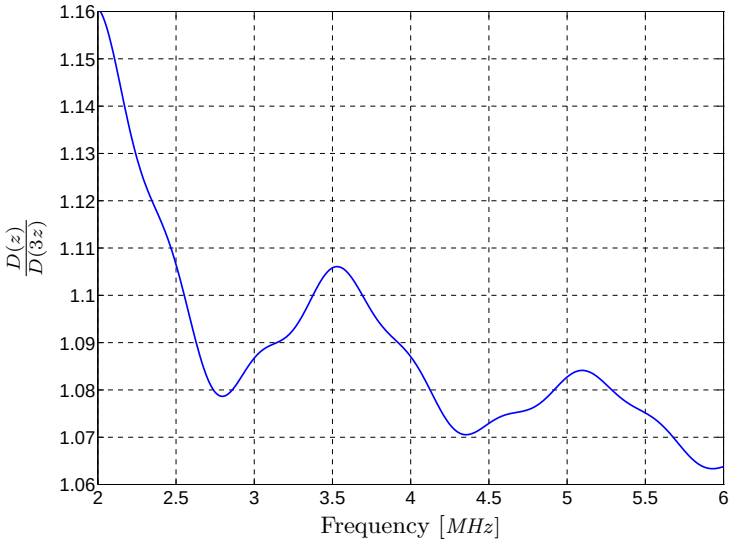

Figure 4.8: Diffraction correction for cement paste

in addition to the material attenuation. These two effects need to be compensated for in the analysis of the attenuation coefficient in order to isolate the material attenuation from those other effects. Inspection of Eq. 4.4(b) quantitatively shows the influence of the diffraction effects. Since $\frac{D(z)}{D(3z)} > 1$, $\ln\left(\frac{D(z)}{D(3z)}\right) > 0$, i.e. the incorporation of diffraction effects yields a lower attenuation coefficient. Figure 4.8 shows the ratio $\frac{D(z)}{D(3z)}$ as a function of frequency for cement paste.

4.3.2 Comparison of Diffraction and Reflection Coefficient Influences

While only the incorporation of both, reflection and diffraction effects leads to correct results in attenuation measurements, a short comparison of both influences is provided. The influence of the diffraction correction is shown in Figure 4.9 which also includes a non-reflection corrected result for further comparison.

Obviously, the influence of the reflection coefficient is more dominant when compared to diffraction effects which can be explained mathematically with the lower magnitude of the reflection coefficients compared to the ratio $\frac{D(z)}{D(3z)}$. Physically, it means that the influence of the coupling and clamping conditions which essentially define

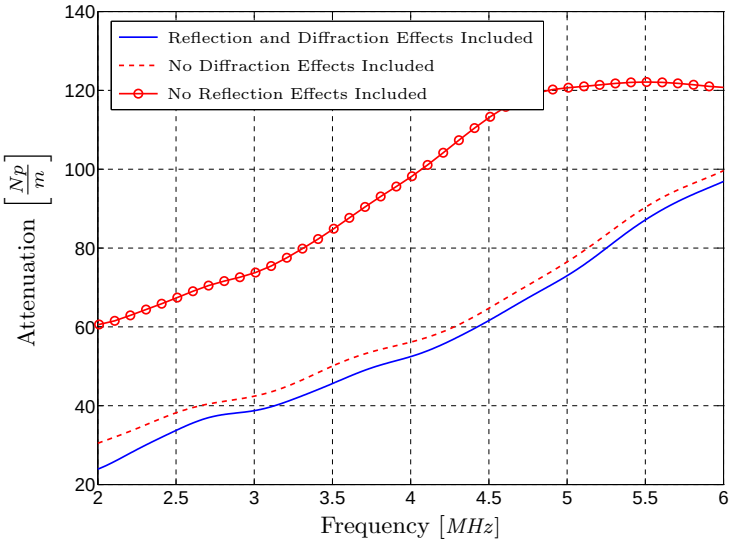

Figure 4.9: Influence of diffraction and reflection coefficients

the reflection coefficient, can give rise to higher errors in attenuation measurements than beamspreading effects if they are not properly accounted for. However, both effects play an important role and should be included in the data analysis.

4.4 A Combined Measurement Procedure

In general, contact attenuation measurements are challenging to perform and researchers have tried various approaches in order to deal with the extraneous influences that affect the measurement and hence the measurement results [32]. Especially, the influence of the transducer clamping and its coupling to the specimen is a source of uncertainty and can therefore give rise to large variations among measurements performed. Even though it is possible to gain control over the governing influential parameters, it might be cumbersome to exactly reproduce a certain coupling and clamping situation. Another more convenient approach is to measure these conditions for each specific measurement setup, and then include the data into the signal processing workflow of the measurement. As it was shown before, the knowledge of the reflection coefficients provides that quantitative measure.

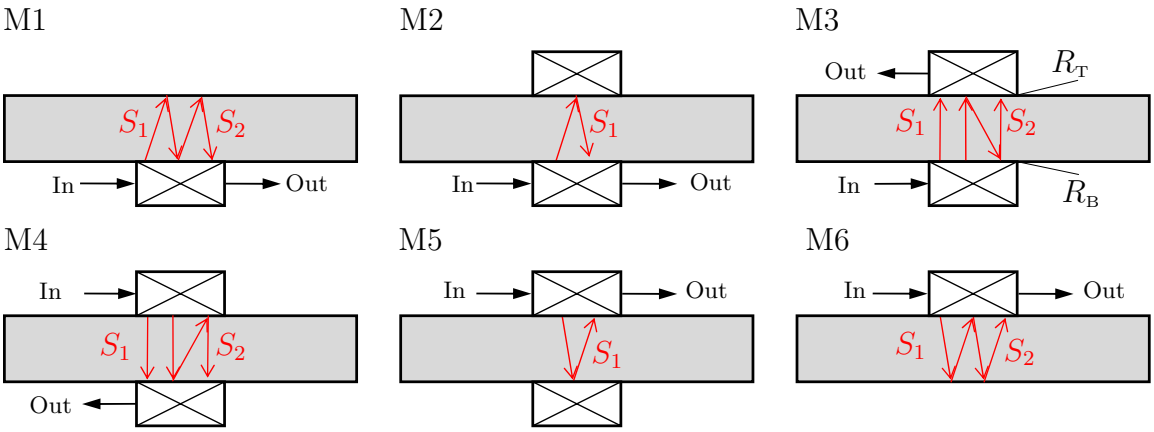

Figure 4.10: Six step measurement procedure

Yet, the measurement of the reflection and attenuation coefficients cannot be performed in a one step setup. To solve that problem, this research develops a combined measurement procedure that follows a sequence of measurements that combine setups with one and two transducers. This sequence allows the evaluation of the reflection coefficients as they are present in the performed attenuation measurement.

The scheme of the measurement sequence is depicted in Figure 4.10 and explained in more detail in the following sections. Note that all measurements are performed with the equipment described in Section 4.1. Between each of the measurement steps, it is crucial to perform the required changes in a way that as few disturbances as possible are introduced into the setup. Of specific importance is the use of a mechanical fixture that allows holding the position constant and to fix both transducers to the specimen seperately. No changes concerning the coupling and clamping are made unless the subsequent step requires a different setup.

4.4.1 Measurement Sequence Steps

In the first step M1, a one transducer setup is used in the pulse echo mode to determine the first two echoes from the free upper surface.

Next, in the second step M2, the upper transducer is mounted onto the specimen but has no electrical function at that point. Again, the lower transducer works in a

pulse echo mode to record the reflected signal from the surface that now includes the transducer reflection effects.

Connecting the upper transducer with the receiving amplifier for the third step M3 yields the first through transmission attenuation measurement setup. The signals that are recorded are the directly transmitted signal and the signal of the wave that reflects on both surfaces of the specimen. Note that due to the shorter propagation distances, the through transmission setups usually require a lower amplification rate than the pulse-echo setups.

Before the fourth step M4, the functions of the incident and receiving transducer are switched, i.e. the wave now travels in the opposite direction. The recorded signals coincide with the ones from the preceeding step.

In the fifth step M5, the incident transducer is again the upper one that now works in a pulse-echo mode to record the reflected signals from the clamped surface of the lower transducer.

The last step M6 is another free surface measurement with the upper transducer as the incident. Before the signals that coincide with the first step are recorded, the lower transducer is removed and some remaining coupling oil is carefully wiped away to guarantee a clean free surface.

Notice that from step two to step five, no change in the clamping or coupling is made to either one of the transducers. Solely, the function of the generating and detecting transducers is interchanged between the third and the fourth step.

4.4.2 Resulting Data

The described measurement sequence provides all the necessary information to analyze the material attenuation of the specimen under consideration. The general signal processing scheme and the resulting data are explained in the following. For better understanding, the respective signals are denoted firstly with their measurement step

and secondly with their signal number. As an example, M3-S1 denotes the signal S1 obtained in the third measurement step.

The signal processing sequence starts with the analysis of the reflection coefficients since these are necessary to subsequently calculate the attenuation coefficients. In order to determine the upper reflection coefficient R_{T}, the spectra of the signals M2-S1 and M1-S1 are compared to each other. Both signals describe the first echo of the wave that was launched by the same lower incident transducer in the same material. Since the only difference is the non-free surface condition due to the upper transducer, the reflection coefficient of the upper surface can be calculated using the signal processing technique described in Section 4.2. Analogously, comparison of the signals M5-S1 and M6-S1 yields the reflection coefficient R_{B} of the clamped surface of the lower transducer.

Knowing the reflection coefficients for the upper and the lower surfaces, the actual attenuation measurement is being performed in steps three and four. Following the steps described in Section 4.1, analysis of signals M3-S1 and M3-S2 yields the material attenuation measured in the through transmission setup. Analogously, signals M4-S1 and M4-S2 yield the same results for the material attenuation. Theoretically, for a perfectly homogeneous and isotropic material, the two results from measurement M3 and M4 should be exactly the same. In practice, due to some external influences and inhomogeneities in the material, this does not exaclty hold true. Nevertheless, in all measurements performed in this research, these two results are very close to each other. It can be argued that the third and fourth steps in the measurement sequence are redundant. However, for the investigation of another measurement technique, both steps were carried out in the current research.

As a byproduct of the described technique, measurement steps M1 and M6 provide

two more attenuation measurements. With the knowledge of both reflection coefficients, comparison of signal M1-S1 with M1-S2 as well as comparison of M6-S1 with M6-S2 can be used to evaluate the material attenuation for the double echo measurement setup.

In conclusion, the proposed combined measurement setup provides the knowledge of both reflection coefficients defining the current clamping and coupling conditions. These coefficients are then used in the actual attenuation calculations using the data from measurement steps three and four and from steps one and six for the through transmission and the double echo method, respectively.
Hence, the method provides four attenuation results for one position of the specimen. While these results ideally should be identical, averaging over the four slightly varying results yields a very good approaximation of the actual material behavior.

4.5 Reference Measurement on a PMMA Specimen

To demonstrate the accuracy of the proposed technique, a reference measurement is performed on a polymethylmethacrylate (PMMA) specimen (referred to as Lucite) of 25.4mm thickness. Comparable data for this material can be found in the literature. Reliable attenuation measurements have been performed by Jarzynski and Hartmann [8] and by Cheeke [5].

4.5.1 Results

Figure 4.11 shows the measured reflection coefficients for the upper and lower transducer-specimen pairings. The previously discussed drop around the center frequency of the 5 MHz transducer is clearly recognizable. Note that for the following analysis, it is not necessary that both reflection coefficients are in a comparable range. However, comparable values represent similar coupling and clamping conditions on the top and

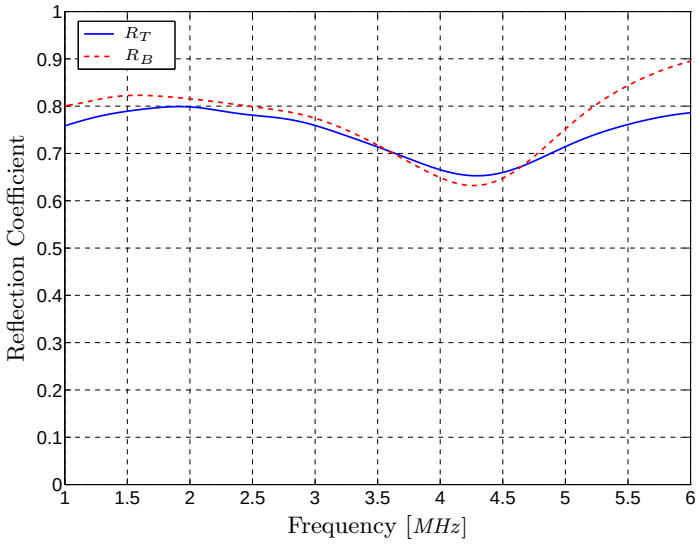

Figure 4.11: Reflection coefficients for Lucite

bottom of the specimen which is generally favorable regarding the repeatability of the measurements.

Figure 4.12 depicts the dispersion curve of Lucite. It can be seen that the material is nearly nondispersive, i.e. the longitudinal phase velocity can be assumed to be constant over a large frequency range ($2\ MHz \leq f \leq 6\ MHz$).

The resulting four attenuation coefficients from the combined measurement sequence are summarized in Figure 4.13. The errorbars depict the variation among the four measurement sets while the solid line and the markers denote the average over all values for each frequency. These values are fitted with a linear regression shown in Figure 4.14. The linear fit is given by

$$\alpha = -2.68 \left[\frac{Np}{m}\right] + 12.8 \left[\frac{Np}{m \cdot MHz}\right] \cdot f \,. \tag{4.10}$$

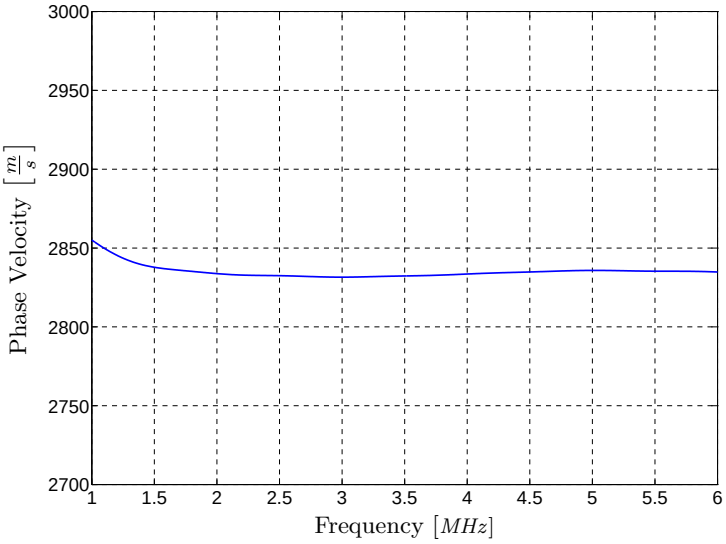

Figure 4.12: Longitudinal phase velocity for Lucite

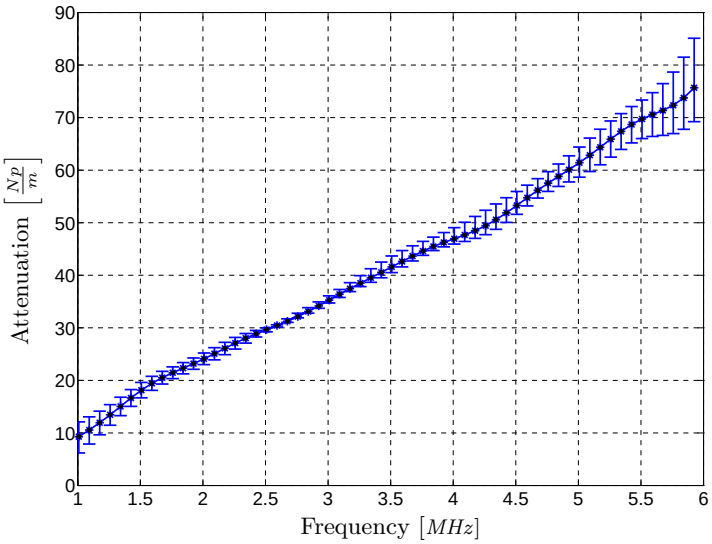

Figure 4.13: Longitudinal attenuation for Lucite

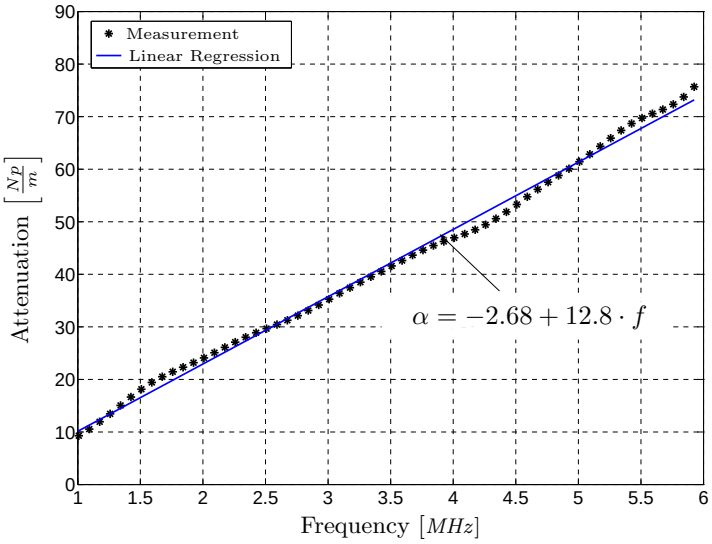

Figure 4.14: Linear regression for longitudinal attenuation for Lucite

4.5.2 Comparison to Published Values

For the Lucite material considered in this research, a longitudinal phase velocity of $c_{\mathrm{L}} = 2835\frac{m}{s}$ is found. This is close to the published values of $c_{\mathrm{L}} = 2690\frac{m}{s}$ by Jarzynski [8] and $c_{\mathrm{L}} = 2750\frac{m}{s}$ by Cheeke [5]. The variations can be explained with typical variations among Lucite materials.

As it can be seen in Figure 4.14, the longitudinal attenuation of Lucite can be well approximated by a linear function. Previously mentioned, this behavior can be explained with the hystersis absorption that is usually found in polymer materials. This hysteresis absorption is characterized by the equation $\alpha\Lambda = const$. Considering only the second term of Eq. 4.10, which denotes the major component of the attenuation coefficient, the attenuation per wavelength can be found to be

$$\alpha\Lambda = 12.8 \cdot f \cdot \frac{c_L}{f} = 12.8 \cdot c_L \approx 0.036Np\,. \tag{4.11}$$

This, again falls well in the range of published values, that show a large variation. Jarzynski finds $\alpha\Lambda = 0.022Np$ while Cheeke finds $\alpha\Lambda = 0.045Np$.

The demonstrated reference measurement on a well known material shows the robustness and accuracy of the proposed measurement procedure.

4.6 Specimens

This research investigates the behavior of two types of materials. The first type are pure cement paste specimens while the second type are cement paste specimens that contain varying amounts of different inclusions.

This section describes the specimens used in this research. After the casting procedure and the type of inclusions are explained, the method to determine the actual volume fraction of inclusions is provided and the specimen data is summarized.

4.6.1 Casting Procedure and Finishing

The basic material for both specimen types is cement paste that is cast from commercial type I Portland cement powder into cylinders of $76.2mm$ diameter. The cement powder is mixed with water, at a water to cement mass ratio of $\frac{w}{c} = 0.4$ utilizing a Hobart mixer before a vibration table is used to diminish the amount of entrapped air in the material. Note that any aggregate is mixed with the cement powder before contacting it with water in order to assure proper mixing conditions for the aggregate. After 24 hours of hydration time in an airtight environment the specimens are hard enough to be demolded. For another 14 days, they continue the hydration process in a water bath where calcium hydroxide is added in order to decrease the amount of leaching of calcium hydroxide from the cement itself and to prevent cracking that arises from a chemical alkali-silica reaction (ASR) between the inclusions and the cement paste [15].

From the demolded cylinders, various specimens are cut with a water cooled diamond saw. After the sawing process, the specimens are polished with a diamond polishing paper to guarantee plane and parallel surfaces that provide a suitable contact between the transducer and the specimen. It has been shown that the roughness of the

coupling surface is important in order to allow for the transfer of the wave energy into the specimen [33]. To dry the specimens after the polishing process, they are kept in a drying oven at 40°C for twelve hours. Note that between each measurement the specimens are kept in an airtight box at room temperature.

4.6.2 Inclusions

In this research, specimens with various types of inclusions are cast in order to get a sense of the acoustic behavior of particulate materials with different types of inclusion materials.

The most important samples contain varying amounts of non-reactive sand, i.e. sand that has undergone chemical treatment in order to prevent ASR cracks at the interface with the cement paste matrix material. The sand is sieved between two sieves with nominal grid sizes of $0.76mm$ and $0.841mm$ to yield a size distribution between these values. For further investigation, especially regarding the modeling techniques, the radius of the sand inclusions is assumed to be $a = 0.4mm$ and is identical for all sand grains. The grains itself are assumed to be spherical in shape.

Two other specimen types are cast with varying amounts of beads made from alumina (Al_2O_3) and borosilicate glass with diameters of $1mm$ and $2mm$, respectively. Unfortunately, these specimens show a material attenuation that is too high, so no reliable attenuation results were determined due to poor SNR. Moreover, alumina shows a very poor workability especially in the grinding process due to its extreme hardness.

4.6.3 Volume Fraction Analysis

During the casting procedure, the possibilities of controling the volume fraction of inclusions are limited. Even though a specific volume fraction for each specimen is aimed for during the process, due to shrinking and hydration effects it cannot be guaranteed that this volume fraction represents the actual one in the hardened

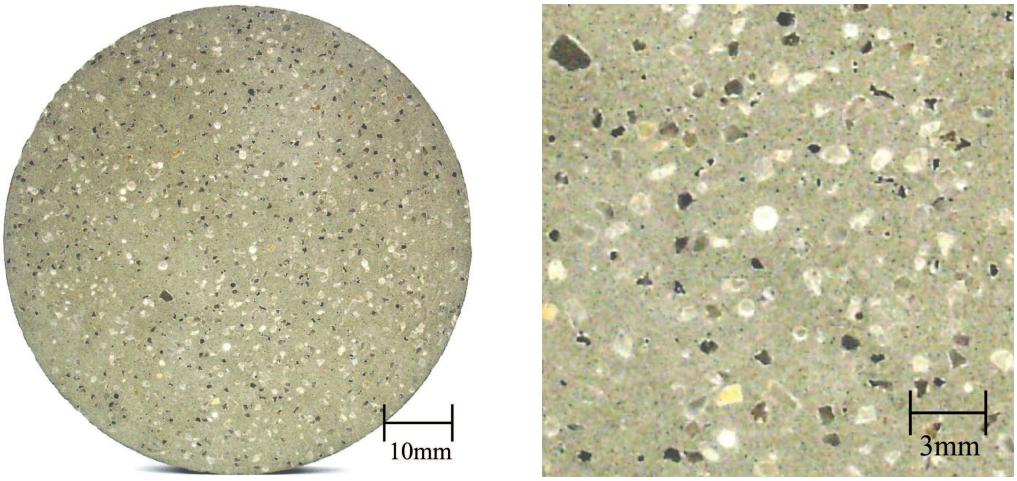

Figure 4.15: Mortar specimen with 9% sand inclusions

specimens. For that reason, a suqsequent analysis is performed which is based on density measurements. Density measurements are carried out by measuring the mass and volume of the specimen. Using the cement paste's density, ρ_{CP} and comparing it to the density ρ_{Sp} of the specimen with inclusions of density ρ_{Inc}, the actual volume fraction η for each specimen can be determined.

Application of the conservation of mass yields

$$\rho_{\text{Sp}} = (1-\eta)\rho_{\text{CP}} + \eta\rho_{\text{Inc}} \,, \tag{4.12a}$$

from which the actual volume fraction is found to be

$$\eta = \frac{\rho_{\text{Sp}} - \rho_{\text{CP}}}{\rho_{\text{Inc}} - \rho_{\text{CP}}} \,. \tag{4.12b}$$

4.6.4 Specimen Data

The general appearence and a closer look at the surface of the 9% mortar specimen is depicted in Figure 4.15.

The corresponding data for each specimen used in this research is summarized in Table 4.1. Note that not all of these specimens are used for analysis in this research. However, for completeness and for further investigation, all specimens are described

Table 4.1: Specimen properties

Specimen	**Inclusion Type**	$\frac{\mathbf{w}}{\mathbf{c}}$ **- Ratio**	**Thickness [mm]**	**Mass [g]**	**Inclusion Size [mm]**	$\boldsymbol{\eta}$ [%]
CP I	-	0.4	11.3	102.6	-	-
CP II	-	0.4	12.3	110.7	-	-
CP III	-	0.4	10.7	97.5	-	-
Sand 9	Sand	0.4	12.3	114.2	≈0.4	9
Sand 16	Sand	0.4	11.3	107.1	≈0.4	16
Sand 18.5	Sand	0.4	12.3	117.5	≈0.4	18.5
Alu 8.0[3]	Al_2O_3	0.4	10.8	104.7	1	8.0
Alu 8.4[3]	Al_2O_3	0.4	12.4	120.6	1	8.4
Glass 9.4[3]	Glass	0.4	12.7	115.2	2	9.4
Glass 9.8[3]	Glass	0.4	13.5	122.8	2	9.8

and their sepcific data is summarized.

[3]Specimen not used in the current research

CHAPTER V

RESULTS

In order to obtain the attenuation curves for the considered materials, the attenuation coefficients of the described specimens are measured using the proposed measurement technique. In this chapter, the results of the attenuation measurements are presented and discussed. It starts with the measurement of the pure cement paste specimens, since this attenuation data defines the matrix absorption of the particulate composite materials and is therefore an important input parameter for the theoretical models. In the next step, the mortar specimens with varying amount of sand inclusions are measured and compared to each other. Finally, the measured attenuation is compared to the two different model predictions evaluated in this research. Differences among the models and the overall accuracy of the model predictions are discussed. The chapter ends with a theoretical approach to model the attenuation behavior of a three-phase material system based on a cement paste matrix containing sand inclusions and air voids. In order to do so, the two different models are expanded and combined. The general results and a comparison between the models and combinations is provided.

5.1 Cement Paste Specimens

The three cement paste specimens were measured using a pair of 5 MHz transducers in the previously defined measurement procedure. The measured values are the frequency dependent longitudinal phase velocity and the attenuation coefficient for a longitudinal wave.

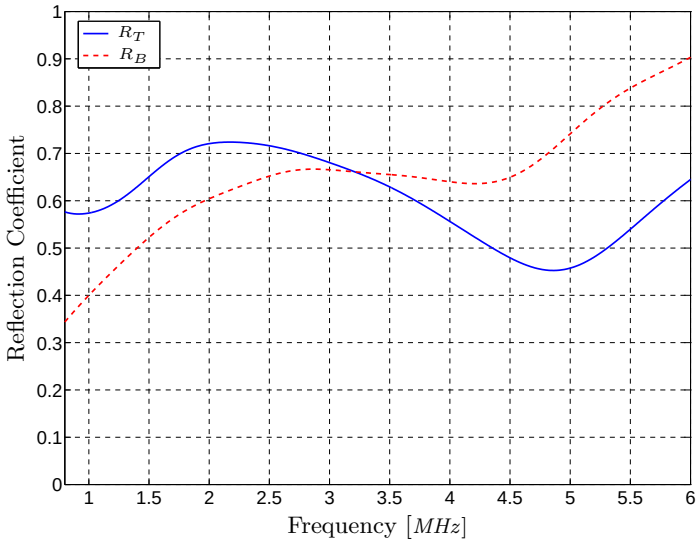

Figure 5.1: Reflection coefficients for cement paste

Typical reflection coefficients for cement paste transducer pairings are shown in Figure 5.1. Note that for all the measurements carried out, the magnitude of the reflection coefficients for the cement-based materials is slightly smaller than for the Lucite specimen. This behavior can be explained with the impedance mismatch between the transducer and the specimens. However, the reflection coefficients for all cement-based materials fall within a similar range of values. Therefore, no reflection coefficients are shown for the following measurements.

A typical dispersion curve for cement paste is shown in Figure 5.2. Very little variation among the different measurements is observed for the cement paste specimens. It can be seen that in the investigated frequency range, cement paste is nearly nondispersive i.e. the phase velocity is nearly constant over a large frequency band (i.e. $2MHz \leq f \leq 6MHz$). The higher phase velocities in the low frequency range refer to a convergence problem in the signal processing. Thus, for the input parameter of the models, the longitudinal phase velocity is assumed to be constant at a value of $c_{\mathrm{L}} = 3680\frac{m}{s}$. This value is comparable to measurements carried out by Punurai

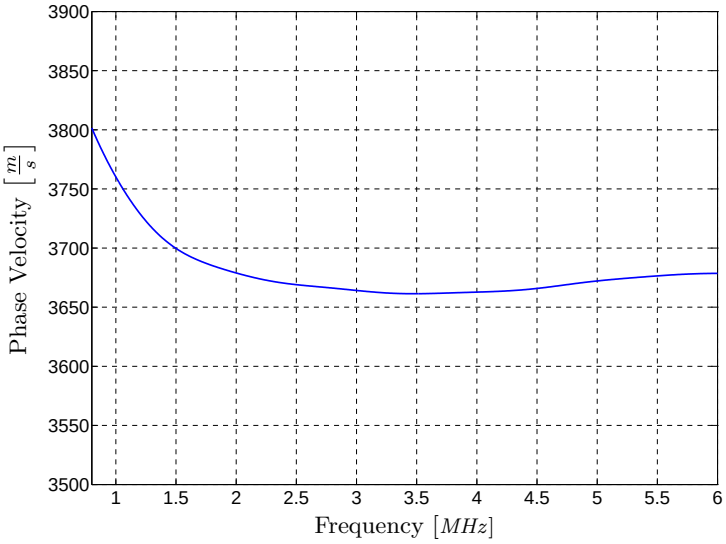

Figure 5.2: Longitudinal phase velocity for cement paste

et al. [25] who finds a nearly constant wavespeed of $c_{\mathrm{L}} = 3750\frac{m}{s}$ even in a lower frequency band.

In order to determine the material attenuation for cement paste, the three specimens were measured and the resulting attenuation curves are averaged. Regarding the four attenuation results that are determined by each measurement procedure, Figure 5.3 shows the mean values and error bars of twelve measurements that provide reliable information about the material behavior.

It is observed that the attenuation coefficient increases linearly with frequency. This behavior can be explained with the hysteresis absorption phenomenon that is also observed by Punurai et al. [25] and is present in many materials such as polymers. Figure 5.4 shows the mean values for the attenuation coefficent and the linear regression that is used for the model calculations. The fit is given by

$$\alpha = -10.19 \left[\frac{Np}{m}\right] + 16.18 \left[\frac{Np}{m \cdot MHz}\right] \cdot f \,. \tag{5.1}$$

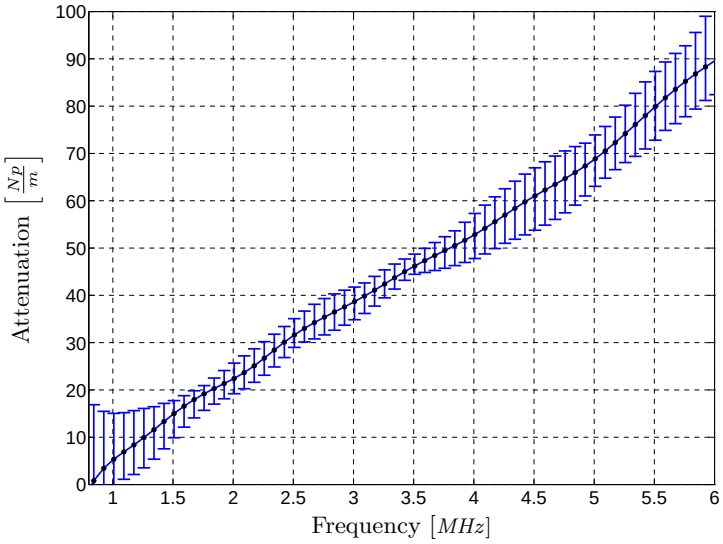

Figure 5.3: Longitudinal attenuation for cement paste

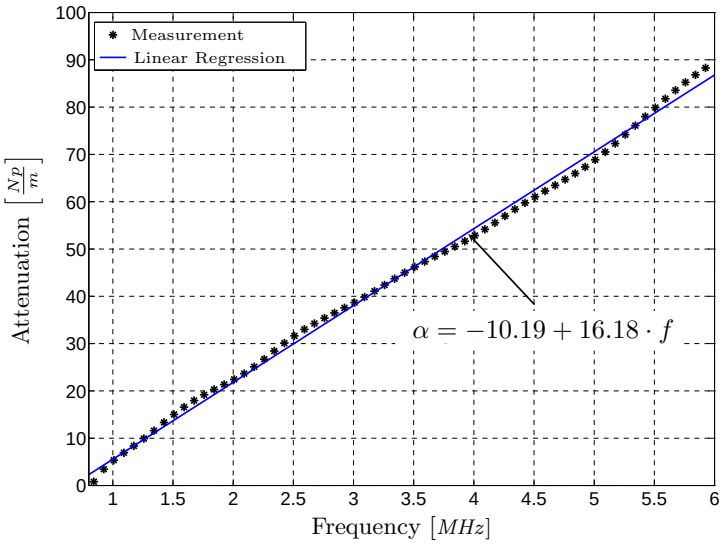

Figure 5.4: Linear regression for longitudinal attenuation for cement paste

5.2 Mortar Specimens

Due to the higher attenuation in the particulate mortar material, the three specimens are measured in a lower frequency range, i.e. they are measured using the 2.25 MHz center frequency transducers. The investigated frequency range depends on the magnitude of the second signal that is analyzed. For higher amounts of inclusions, the material attenuation increases significantly, resulting in a smaller frequency band that is securely covered by the transducer's efficiency.

In general, it is observed that the SNR for the more complex material increases, especially for the structural noise that is due to scattering effects of the inclusions close to the surface. For higher frequencies, this effect prevents the identification of a clear second signal which is necessary in order to perform attenuation measurements.

In all mortar specimens, a normal spatial distribution of the sand inclusions is assumed. This assumption becomes more realistic if an average over different positions on the specimen is calculated. The represented attenuation coefficients and their respective errorbars refer to measurements that were carried out at three different positions on each specimen.

5.2.1 9% Sand Specimen

Figure 5.5 shows the attenuation coefficient for the specimen including 9% sand in the cement paste matrix. Several observations are made regarding the measured attenuation. Firstly, it is observed that the variations between the measurements are larger compared to the pure cement paste. This behavior can be attributed to to the inhomogeneity of the considered material. Secondly, the plot shows negative attenuation coefficients for some measurements in the low frequency range. Physically, these values do not make sense since they would indicate an amplification of the wave amplitude that obviously does not take place. However, the negative values can be explained mathematically with the fact that the reflection coefficient correction is

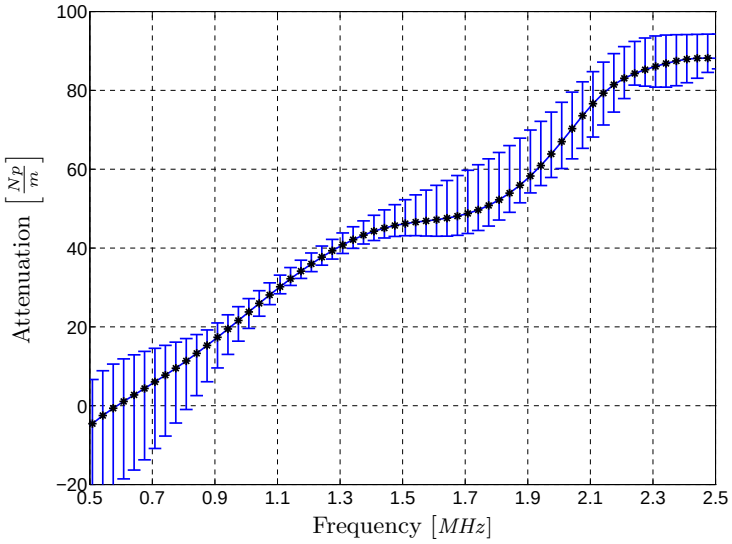

Figure 5.5: Longitudinal attenuation for 9% sand specimen

larger than the spectral ratio of the two considered signals. Physically, the behavior can be explained with an insufficiently strong second signal, especially for the double echo measurements. In the low frequency range, the bandwidth of the utilized transducers is not sufficient in order to get a high SNR. However, since the through transmission setups deliver reliable results, these are included in the plot.

5.2.2 16% Sand Specimen

The longitudinal wave attenuation coefficient and the respective errorbars for the 16% sand containing specimen are shown in Figure 5.6. It is primarily observed, that the attenuation for the specimen containing higher amounts of inclusions is higher which coincides with the predictions from the theoretical models. The higher number of scattering inclusions results in higher attenuation coefficients. The negative values in the low frequency range again refer to an insufficient amount of incident signal, especially for the double echo setups.

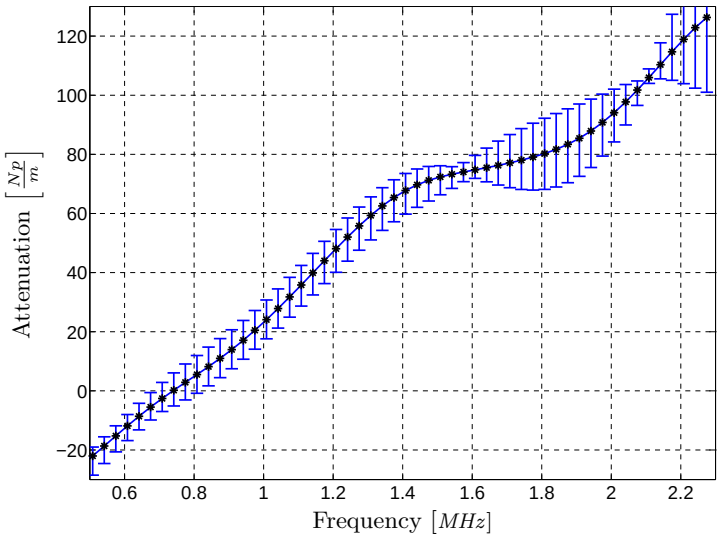

Figure 5.6: Longitudinal attenuation for 16% sand specimen

5.2.3 18.5% Sand Specimen

Figure 5.7 shows the results of the performed attenuation measurements on the 18.5% sand containing specimen. Large variations among the different measurements and positions are observed which indicate the high amount of inhomogeneity present in the material. The variation is significantly strong in the frequency range around 1.7 *MHz* which falls into the resonance range of the measuring transducers. Thus, it is most probable that the high variation is due to differences in the coupling conditions that are not completely eliminated by the reflection coefficient correction.

5.2.4 Comparison of Mortar Specimens

The comparison of the three investigated mortar specimens is shown in Figure 5.8. For further information, it also contains the cement paste absorption. As expected, the effect of the inclusions is a higher attenuation over the whole frequency band. Moreover, these effects become more important for higher frequencies i.e. for wavelengths which are in the range of the scatterer size or smaller.

Comparison of the mortar specimens shows clearly, that a higher amount of inclusions

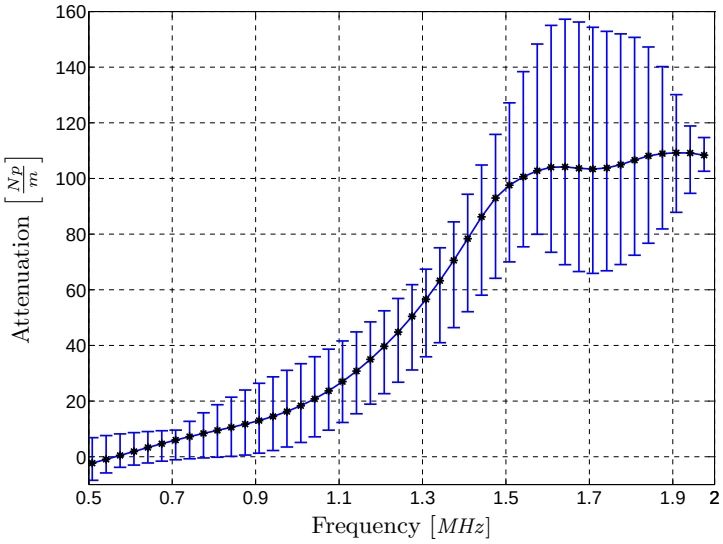

Figure 5.7: Longitudinal attenuation for 18.5% sand specimen

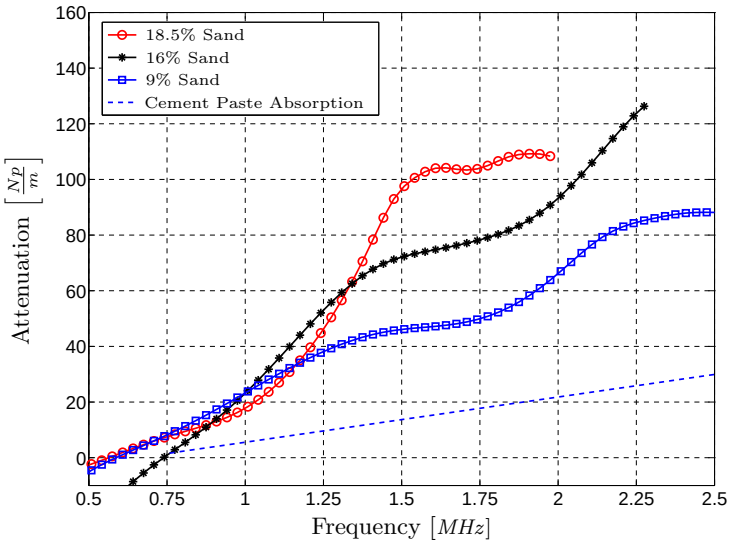

Figure 5.8: Comparison of mortar specimens

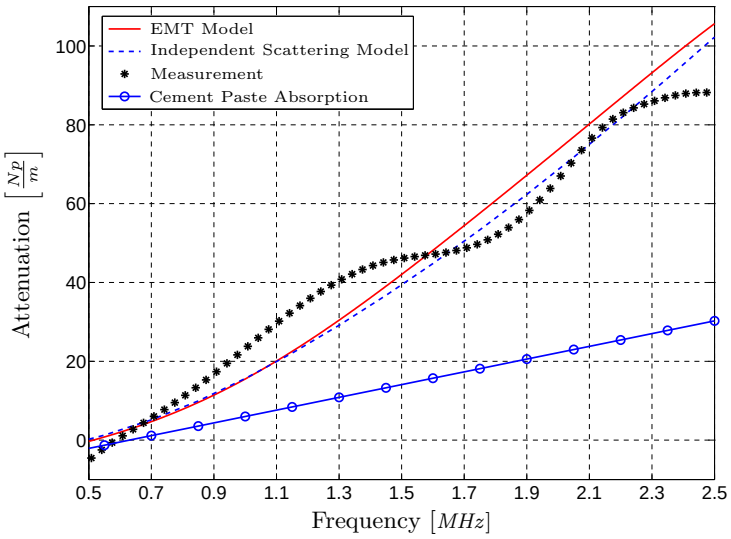

Figure 5.9: Comparison of models and measurement for 9% sand specimen

result in higher attenuation. Interestingly, the rise in attenuation from the 9% specimen to the 16% specimen is very comparable to the rise in attenuation from the 16% specimen to the 18.5% specimen, even though the difference in the inclusion amount is considerably smaller. This behavior can best be explained with the accuracy of the measurement setup. Regarding the large variations among the measurements, no exact interpretation is reliable in this frequency range.

5.3 Comparison to Model Predictions

In this section, the results of the mortar specimens are compared to the different model predictions and the respective agreement is discussed.

5.3.1 9% Sand Specimen

Figure 5.9 shows the comparison of the averaged measurement values to the two model predictions. For further evaluation of the scattering effects, the pure cement paste absorption is also depicted. Good agreement is observed between both model predictions and the measured values over the whole frequency band. A slight underestimation of the predicted attenuation is observed in the frequency band between

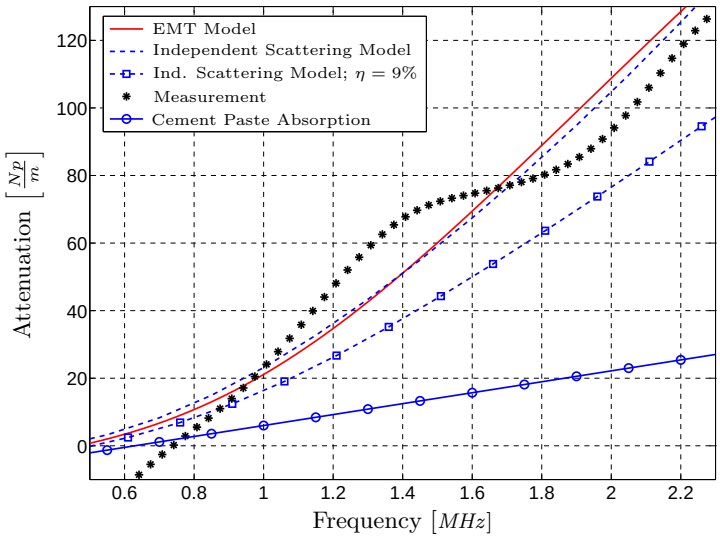

Figure 5.10: Comparison of models and measurement for 16% sand specimen

1 *MHz* and 1.5 *MHz*. A lower attenuation coefficient resulting from the measurements around 2.5 *MHz* is observed in comparison to the model values.

Moreover, the comparison shows that there are only small differences among the two models in the investigated frequency band. Generally, the EMT model predicts higher attenuation values for nearly the whole frequency range. This refers to the capability of modeling scatterer interactions that result in higher attenuation. Regarding the measurement data, none of the different models shows a clearly better prediction of the material behavior. Apparently, the effect of scatterer interactions is not dominant for the investigated volume fraction and frequency band.

5.3.2 16% Sand Specimen

For the case of the 16% sand specimen, the comparison between the model predictions and the measurement data is shown in Figure 5.10. Again, there is good agreement between both model predictions and the measured material attenuation, especially in the higher frequency range. Interestingly, the pattern of differences is similar to that of the lower volume fraction case, showing an underestimation of the models

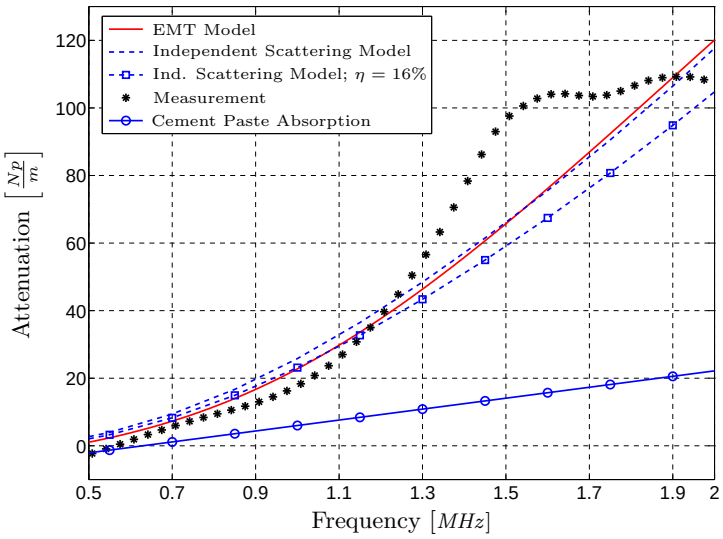

Figure 5.11: Comparison of models and measurement for 18.5% sand specimen

in the lower range while the predictions show higher values in the higher frequency range. Both models again do not show large differences in the investigated frequency range. For further comparison, Figure 5.10 also depicts the independent scattering model prediction for the lower volume fraction specimen. Even though there is some deviation for the 16% volume fraction models and the measurement data, it is observed that these models fit the measurement data in a more accurate fashion than the depicted 9% model, i.e. both models correctly represent the higher attenuation due to the higher amount of inclusions.

5.3.3 18.5% Sand Specimen

Figure 5.11 shows the results of the 18.5% sand specimen. There is good agreement between the measurement data and both model predictions with best results in the range of 0.5 *MHz* to 1.2 *MHz* where in both models the attenuation is constantly overestimated by a small amount. However, this overestimation falls into the range of the accuracy of the measurement system. Again, both models do not differ enough in order to quantify and compare the accuracy of both models.

The differences between the model predictions and the measurement are the largest in the range between 1.5 MHz and 1.7 MHz. This coincides with the range of large variations among the measurements, compare to Figure 5.7. Consequently, the measurement data are not so reliable that any physical interpretations are possible. Most probably, the peak which is not present in both model predictions relates to a transducer resonance phenomenon that is not completely corrected.

The model results of the independent scattering model for the case of $\eta = 16\%$ is also depicted in Figure 5.11. It is observed that especially in the low frequency range where there is good agreement with the measurement result, the models are in the same range. Thus, the sensitivity of the model towards small changes of the input paramter η is not sufficient in order to clearly distinguish measurement data from specimens with slightly different amounts of inclusions. As was shown before, larger variations of the volume fraction can be distinguished by both models.

5.4 Modeling of Three-phase Materials

The models described in the Chapter 3 have shown the capability to predict the ultrasonic wave attenuation for a two-phase material, i.e. a homogeneous matrix with spherical inclusions. To develop a better model of real concrete, it is desirable to incorporate multi-phase materials. The following section describes how the independent scattering and EMT model can be expanded and combined to approach the attenuation modeling for three-phase materials, i.e. cement paste, elastic inclusions and air voids. Note that for these materials no experimental data exists at the present time.

All models again assume a viscoelastic cement paste matrix material with spherical inclusions of volume fractions η and ϕ for the elastic inclusions and the air voids, respectively. At this point, no size distribution of the elastic inclusions or the air voids is taken into account.

The models and combinations and their capabilities are first described before the resulting attenuation coefficients are compared to each other.

5.4.1 Multiphase Independent Scattering Model

The independent scattering model previously described is extended to include cavities in cement paste by adjusting the formulations for the scattering cross section. This technique was used in [25] to model air voids in cement paste. In order to yield a formulation for a three-phase material, Eq. 3.1 is extended to

$$\alpha = (1 - \eta - \phi)\alpha_a + \frac{1}{2} n_s^{\text{Inc}} \gamma_{\text{Inc}}^{sca} + \frac{1}{2} n_s^{\text{Air}} \gamma_{\text{Air}}^{sca} \,, \tag{5.2}$$

where n_s^{Inc} and n_s^{Air} represent the respective number of scattering elastic inclusions and air voids per unit volume while $\gamma_{\text{Inc}}^{sca}$ and $\gamma_{\text{Air}}^{sca}$ denote their respective scattering cross sections. Formulations for $\gamma_{\text{Inc}}^{sca}$ and $\gamma_{\text{Air}}^{sca}$ are attached in Appendix A.

The extended independent scattering model represents an approximation to model the acoustic behavior of a three-phase material which does not take any kind of scatterer interactions into account. The model can easily be extended to a multiphase material if the total volume fraction of inclusions is relatively low.

5.4.2 Effective Medium Theory and Indendent Scattering Model

Another modeling approach uses the effective medium theory to find the effective attenuation coefficient for cement paste containing only elastic inclusions, Eqs. 3.5 - 3.7. After this homogenization process, the effective attenuation coefficient is taken as an input parameter for the independent scattering model defining the absorption of the matrix with the elastic inclusions. The attenuation of the overall three-phase material can then be calculated using the formulae for the independent scattering model, Eq. 3.1, to incorporate the air voids.

The combination of the EMT model followed by the independent scattering model results in a specific capability of modeling scatterer interactions. Since the effective media model takes interactions of the elastic inclusions into account, the combined theory also accounts for these interactions. For this combination, no further obstacle interactions (i.e. between air voids themselves or air voids and inclusions) can be modeled.

5.4.3 Two Step Effective Medium Theory

The second model also follows a two step sequence starting with the homogenization of the cement paste and the elastic inclusions. In a next step, the calculated effective elastic constants and density of that particulate material are taken as input parameters for another evaluation of the effective media model. In this second step, the inclusion properties are taken to be zero-valued to model the behavior of air voids in which no wave propagation is assumed to be possible. The resulting elastic constants after the second step are combined to calculate the overall material attenuation using Eqs. 3.11 - 3.16. Therefore, the model can be described as the subsequent modeling of two two-phase materials.

Since the EMT apporach is used in both steps of the calculation, the model is capable of representing scatterer interactions in both of these steps. As a result, the attenuation due to interactions between the elastic inclusions themselves, and air voids themselves is taken into account to some degree. However, any wave scattering interactions that might occur between elastic inclusions and air voids are not fully accounted for due to the lack of coupling between the two steps of the calculation.

5.4.4 Expanded Effective Medium Theory

Sabina and Willis derive their effective medium model for the general case of a matrix material containing N types of inclusions of the same size and material type [30].

Therefore, the implemented model can be expanded to yield expressions for a three-phase particulate material. The expanded formulations can be found in Appendix A.

The expanded EMT model defines a method to integrate a multi-phase material in a one-step calculation. Using the effective medium approach to homogenize the complete material, the model takes all kinds of obstacle interactions into account. These interactions are not directly represented but are implied in the constraint of self-consistency which is the essential assumption for the EMT approach.

5.4.5 Comparison of Three-phase Material Models

Evaluations of the models and combinations for implementing a cement paste matrix containing elastic inclusions as well as air voids are shown in Figure 5.12. The models represent a material with the following data: $\eta = 15\%$, $\phi = 5\%$, $a_{\text{Inc}} = 0.4mm$ and $a_{\text{Air}} = 0.1mm$.

The increase in the attenuation coefficent for the models can be explained by looking at the different obstacle interactions that the respective models account for.

Since the combination of the independent scattering and the EMT model can only represent multiple scattering effects between the elastic inclusions themselves, it results in the lowest attenuation coefficient over the whole frequency range. A slightly higher coefficient is obtained by the two step EMT model. In comparison to the former model, it expands the represented obstacle interactions by the incorporation of multiple scattering between air voids themselves. The interaction between both types of inclusions are only taken into account in the expanded EMT model, yielding the highest attenuation coefficient of all the models including an EMT approach over the whole frequency range.

The expanded independent scattering model is not capable of modeling any kind of

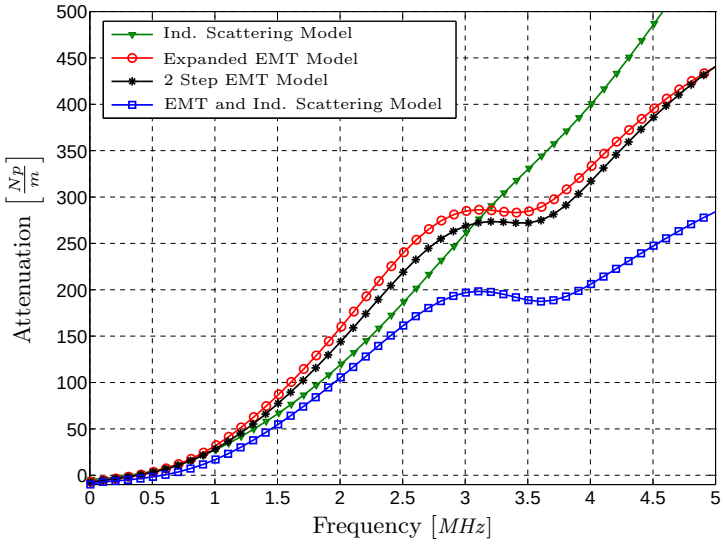

Figure 5.12: Comparison of different models and combinations

scatterer interactions. However, for higher frequencies it shows the highest attenuation coefficient. While this does not make sense from a physical point of view, the generally higher attenuation for the independent scattering model can probably be explained with the different modeling approach for the single scatterer problem. Moreover, the independent scattering model does not show a clear resonance phenomenon in the frequency range around 3 MHz.

The difference between the described models and combinations becomes more and more important when the volume fraction of the inclusions increases. In this case, multiple scattering effects become dominant and it is crucial to include them into the modeling technique in order to get accurate results.

CHAPTER VI

CONCLUSIONS AND OUTLOOK

This chapter summarizes the conducted research and provides an outlook on future applications of the obtained results. An overview of the subsequent work to be carried out is presented.

6.1 Conclusions

This research demonstrates the influence of elastic inclusions in cement-based materials and shows the effectiveness of different scattering models which are used in order to predict the attenuation of longitudinal waves propagating in these particulate materials. The basic mechanisms of scattering attenuation due to sand inclusions in cement paste are investigated in order to expand on the fundamental knowledge of wave propagation in cement-based materials. This knowledge allows for further research towards more realistic material models.

The research applies two existing theoretical models to the case of scattering attenuation due to sand inclusions in a homogeneous cement paste matrix – an independent scattering model as well as a self-constistent effective medium theory based model. While no scatterer interactions are implied in the former model, the latter one takes these multiple scattering effects into account.

The experimental part of this research develops an attenuation measurement technique for highly attenuative, particulate materials based on a combination of contact

measurements combined with spectral ratio signal processing techniques. The research introduces the reflection coefficients between the specimens and the measuring transducers as a way to quantitatively describe the coupling and clamping conditions present in a specific measurement setup. A combined sequence is proposed in order to carry out these analyses as well as the attenuation measurements in an in-situ fashion, thereby significantly reducing variations among different measurements and preventing the attenuation from being overestimated.
This measurement technique allows for the reliable evaluation of the attenuation coefficient of highly attenuative media in a high frequency range.

Next, the attenuation coefficient is measured in a frequency range between 0.5 MHz and 2.5 MHz for mortar specimens with varying amount of sand inclusions and the results are compared to the different model predictions. It is observed that both modeling techniques are in good agreement with the measurement data. Hence, both models show the capability of predicting the material attenuation for the particulate materials considered in this research. Apparently, in the considered frequency range and for the considered amounts of inclusions, multiple scattering effects are not dominant, since only small differences among the models are observed.

Furthermore, the research presents theoretical approaches to model three-phase materials. At this point, no measurement data is present for these types of materials.

6.2 Outlook and Further Work

The research shows that scattering attenuation models have the capability of predicting the material attenuation in particulate cement-based materials for a high frequency range. This allows for the in-situ material characterization of these interesting materials and can lead to NDE or even SHM applictions in the future. The

extension of the fundamental knowledge of the propagation of longitudinal waves in particulate, viscoelastic materials might be employed in other applications. Moreover, the progress in the field of contact attenuation measurement techniques is helpful for a number of applications where the attenuation of highly attenuative media need to be evaluated in a high frequency range.

However, subsequent work needs to be performed in order to achieve these goals. Most importantly, the limits of the presented work need to be determined, i.e. the frequency range and the amount of inclusions in the specimens need to be extended while both issues are of specific interest. The measurement and the comparison to both model predictions in a higher frequency range is interesting in this respect that the models show significant differences only for higher frequencies. Especially the investigation of the resonance phenomenon of the scattering inclusions might present a good measure of the accuracy and applicability of both models. Nevertheless, the inspection of a higher frequency range requires the further development of the current or the invention of a new measurement technique.
The investigation of mortar specimens with higher amounts of inclusions could also provide valuable information about the accuracy and applicability of the described modeling techniques, especially with regard to the influence of multiple scattering effects.

As a next step towards a more realistic model of real concrete structures, measurements on a three-phase material consisting of a cement paste matrix including both elastic inclusions and air voids need to be performed. The presented modeling approaches need to be validated with measurement data and can be further evaluated, different modeling techniques can be applied or new models might be developed.

In order to use ultrasonic wave attenuation as an NDE technique for cement-based materials, the inverse problem needs to be considered where the input parameters to the models are to be found from measurement data. Therefore, the applicability of mathematical inversion techniques need to be investigated in the future.

APPENDIX A

DERIVATIONS FOR ATTENUATION MODELING

This appendix provides some additional information and formulae about the theory of the different models, described in Chapter 3.

A.1 Determination of the Scattering Cross-Section γ^{sca} for Elastic Inclusions and Cavities

The mathematical formulation of the independent scattering model as it is used in this research is given by Ying and Truell [35]. This section briefly describes the fundamental ideas and basic steps in order to calculate the scattering cross-section γ^{sca} necessary to evaluate the attenuation coefficient. First, the derivation for an elastic inclusion is provided before the necessary adaptions and simplifications for the case of a scattering cavity are explained.

A.1.1 Elastic Inclusion

A plane, harmonic, wave is considered in the particulate material. The particle displacement, described in spherical coordinates (r, ϕ, θ) is given by the expression

$$\mathbf{U} = \mathbf{u}e^{i\omega t} \,, \tag{A.1}$$

where the displacement vector $\mathbf{u}$ is defined in terms of the longitudinal displacement potential $\Psi = \Psi(r, \theta)$ as

$$\mathbf{u} = -\nabla\Psi \,. \tag{A.2}$$

It can be shown from the general equation of motion, Eq. 2.7, that for any wave which has a spherical symmetry with respect to the scattering obstacle, the displacement vector $\mathbf{u}$ can be expressed as

$$\mathbf{u} = -\nabla\Psi + \nabla \times [\nabla \times (r\bar{\mathbf{e}_\mathbf{r}}\Pi)] \,, \tag{A.3}$$

with the additional restrictions

$$(\nabla^2 + {k_l}^2)\Psi = 0 \quad \text{and} \quad (\nabla^2 + {k_s}^2)\Pi = 0 \,. \tag{A.4}$$

Here, k_l and k_s define the wavenumbers for a longitudinal and shear wave, respectively while $\bar{\mathbf{e}_\mathbf{r}}$ denotes the unit vector in radial direction.
Generally, the solution of the wave equation is assumed to be of the form

$$\Psi = \frac{1}{k_l}\sum_{m=0}^{\infty}(-i)^{m+1}(2m+1)j_m(k_l\bar{\mathbf{e}_\mathbf{r}})P_m(\cos\theta) \,, \tag{A.5}$$

where $j_m(\xi)$ is the spherical Bessel function of the first kind of order m and P_m is the Legendre polynomial of degree m.

Now, a longitudinal, plane, harmonic wave is considered as the incident wave in the particulate material. Notice that the shear potential $\Pi = \Pi(r,\theta)$ as well as the shear wave number k_s are zero for the considered case of a longitudinal incident wave. When the wave impinges an obstacle of radius a, scattering occurs and both types of waves (longitudinal and shear) evolve inside the inclusion as well as in the surrounding media. Equation A.1 is applicable for all of these wave fields with the respective displacement potentials which are denoted with superscripts (s), (q) and (i) for the scattered, inclusion and incident fields, respectively. For the scattered wave field outside the inclusion, the potentials are expanded as

$$\Psi^{(s)} = \sum_{m=0}^{\infty} A_m h_m(k_l^{(i)}r)P_m(\cos\theta) \,, \tag{A.6}$$

and

$$\Pi^{(s)} = \sum_{m=0}^{\infty} B_m h_m(k_s^{(i)} r) P_m(\cos\theta) \,, \tag{A.7}$$

where $h_m(\xi)$ is the abbreviation of $h_m^{(2)}(\xi)$ and is the spherical Bessel function of the third kind which is related to the cylindrical Bessel function by [20],

$$h_m(\xi) = \sqrt{\frac{\pi}{2}} \, \frac{H_{m+\frac{1}{2}}{}^{(2)}(\xi)}{\sqrt{\xi}} \,, \tag{A.8}$$

$H_{m+\frac{1}{2}}{}^{(2)}(\xi)$ being the cylindrical Bessel function of the third kind.

Even though the wave field inside the inclusion is of no interest for the considered problem, it is needed in order to define the scattered wave field. The inner wave field is defined by the expansions

$$\Psi^{(q)} = \sum_{m=0}^{\infty} C_m j_m(k_l^{(q)} r) P_m(\cos\theta) \,, \tag{A.9}$$

and

$$\Pi^{(q)} = \sum_{m=0}^{\infty} D_m j_m(k_s^{(q)} r) P_m(\cos\theta) \,. \tag{A.10}$$

In order to completely define the scattered wave field, the two parameters A_m and B_m need to be determined. In order to find these, the boundary conditions at the interface between the spherical scatterer and the surrounding matrix material are considered which state that the stress and the particle displacement have to be consistent at all times. For $r = a$ and the case of an elastic inclusion, these boundary conditions are

$$u_r^{(q)} = u_r^{(i)} + u_r^{(s)} \,, \tag{A.11}$$

$$u_\theta^{(q)} = u_\theta^{(i)} + u_\theta^{(s)} \,, \tag{A.12}$$

$$\sigma_{rr}^{(q)} = \sigma_{rr}^{(i)} + \sigma_{rr}^{(s)} \,, \tag{A.13}$$

$$\sigma_{r\theta}^{(q)} = \sigma_{r\theta}^{(i)} + \sigma_{r\theta}^{(s)} \,. \tag{A.14}$$

The displacments u_r and u_θ as well as the stresses σ_{rr} and $\sigma_{r\theta}$ for all the wave fields can be derived from the respective displacement potentials, the respective material

properties and wavenumber. These relations are given by

$$\sigma_{rr} = \rho\omega^2 \left\{ \Psi + \frac{2}{k_s^2} \left[\frac{2}{r}\frac{\partial \Psi}{\partial r} + \frac{1}{r^2}\Omega\Psi - \frac{\partial}{\partial r}\left(\frac{1}{r}\Omega\Pi\right)\right]\right\} , \tag{A.15}$$

$$\sigma_{r\theta} = -2\frac{\rho\omega^2}{k_s^2}\frac{\partial}{\partial\theta}\left[\frac{1}{r}\frac{\partial\Psi}{\partial r} - \frac{1}{r^2}\Psi + \frac{1}{r}\frac{\partial\Pi}{\partial r} + \frac{1}{r^2}\left(1 + \frac{k_s^2 r^2}{2}\right)\Pi + \frac{1}{r^2}\Omega\Pi\right] , \tag{A.16}$$

and for the displacement

$$u_r = -\frac{\partial\Psi}{\partial r}\frac{1}{r}\Omega\Pi \, , \tag{A.17}$$

$$u_\theta = -\frac{1}{r}\frac{\partial\Psi}{\partial\theta} + \frac{1}{r}\frac{\partial^2}{\partial\theta\partial r}\left(r\Pi\right) \, . \tag{A.18}$$

In Eqs. A.15 - A.18, the operator Ω is defined as

$$\Omega = \frac{1}{\sin\theta}\frac{\partial}{\partial\theta}\left(\sin\theta\frac{\partial}{\partial\theta}\right) \, . \tag{A.19}$$

Rewriting the boundary conditions in terms of the definitons of the displacement potentials and rearranging the terms, yield a set of four linear equations to determine the coefficients A_m, B_m, C_m and D_m. These equations are found to be

$$\begin{pmatrix} S_{11} & S_{12} & S_{13} & S_{14} \\ S_{21} & S_{22} & S_{23} & S_{24} \\ S_{31} & S_{32} & S_{33} & S_{34} \\ S_{41} & S_{42} & S_{43} & S_{44} \end{pmatrix} \begin{pmatrix} A_m \\ B_m \\ C_m \\ D_m \end{pmatrix} = e \begin{pmatrix} f_1 \\ f_2 \\ f_3 \\ f_4 \end{pmatrix} , \tag{A.20}$$

with

$$S_{11} = k_l^{(i)} a h_{m+1}(k_l^{(i)}a) \, , \tag{A.21}$$

$$S_{12} = m k_s^{(i)} a h_{m+1}(k_s^{(i)}a) \, , \tag{A.22}$$

$$S_{13} = -k_l^{(q)} a j_{m+1}(k_l^{(q)}a) \, , \tag{A.23}$$

$$S_{14} = -m k_s^{(q)} a j_{m+1}(k_s^{(q)}a) \, , \tag{A.24}$$

$$S_{21} = h_m(k_l^{(i)}a)\,, \tag{A.25}$$

$$S_{22} = -\left[m+1\right]h_m(k_s^{(i)}a) + k_s^{(i)}ah_{m+1}(k_s^{(i)}a)\,, \tag{A.26}$$

$$S_{23} = -j_m(k_l^{(q)}a)\,, \tag{A.27}$$

$$S_{24} = \left[m+1\right]j_m(k_s^{(q)}a) - k_s^{(q)}aj_{m+1}(k_s^{(q)}a) \tag{A.28}$$

$$S_{31} = \frac{(k_s^{(i)}a)^2}{2}h_m(k_l^{(i)}a) - \left[(m+2)(k_l^{(i)}a)\right]h_{m+1}(k_l^{(i)}a)\,, \tag{A.29}$$

$$S_{32} = m\frac{(k_s^{(i)}a)^2}{2}h_m(k_s^{(i)}a) - \left[(m+2)(k_s^{(i)}a)\right]h_{m+1}(k_s^{(i)}a)\,, \tag{A.30}$$

$$S_{33} = -p\frac{(k_s^{(q)}a)^2}{2}j_m(k_l^{(q)}a) + p\left[(m+2)(k_l^{(q)}a)\right]j_{m+1}(k_l^{(q)}a)\,, \tag{A.31}$$

$$S_{34} = -pm\frac{(k_s^{(q)}a)^2}{2}j_m(k_s^{(q)}a) + p\left[(m+2)(k_s^{(q)}a)\right]j_{m+1}(k_s^{(q)}a)\,, \tag{A.32}$$

$$S_{41} = \left[m-1\right]h_m(k_l^{(i)}a) - k_l^{(i)}ah_{m+1}(k_l^{(i)}a)\,, \tag{A.33}$$

$$S_{42} = -\left[m^2 - 1 - \frac{(k_s^{(i)}a)^2}{2}\right]h_m(k_s^{(i)}a) - k_s^{(i)}ah_{m+1}(k_s^{(i)}a)\,, \tag{A.34}$$

$$S_{43} = -p\left[m-1\right]j_m(k_l^{(q)}a) + pk_l^{(q)}aj_{m+1}(k_l^{(q)}a)\,, \tag{A.35}$$

$$S_{44} = -p\left[m^2 - 1 - \frac{(k_s^{(q)}a)^2}{2}\right]j_m(k_s^{(q)}a) - pk_s^{(q)}aj_{m+1}(k_s^{(q)}a)\,, \tag{A.36}$$

where p is the ratio of the shear moduli of the inclusion and matrix material,

$$p = \frac{\mu_{\mathrm{Inc}}}{\mu_{\mathrm{M}}}\,. \tag{A.37}$$

The parameter e is defined as

$$e = (-i)^{(m-1)}(2m+1)\frac{1}{k_l^{(i)}}\,, \tag{A.38}$$

while the right-hand side terms are given by

$$f_1 = k_l^{(i)}aj_{m+1}(k_l^{(i)}a)\,, \tag{A.39}$$

$$f_2 = j_m(k_l^{(i)}a)\,, \tag{A.40}$$

$$f_3 = \frac{(k_s^{(i)}a)^2}{2}j_m(k_l^{(i)}a) - \left[(m+2)(k_l^{(i)}a)\right]j_{m+1}(k_l^{(i)}a)\,, \tag{A.41}$$

$$f_3 = \left[m-1\right]j_m(k_l^{(i)}a) - k_l^{(i)}aj_{m+1}(k_l^{(i)}a)\,. \tag{A.42}$$

Once the expansion coefficients A_m and B_m are found, the scattering cross-section

for the elastic inclusion is found to be

$$\gamma^{sca} = 4\pi \sum_{m=0}^{\infty} \frac{1}{2m+1} \left[|A_m|^2 + m(m+1) \frac{k_l^{(i)}}{k_s^{(i)}} |B_m|^2 \right] . \tag{A.43}$$

A.1.2 Cavity

For the case of a cavity that cannot carry waves of any form, the boundary conditions at $r = a$ are

$$\sigma_{rr}{}^{(i)} + \sigma_{rr}{}^{(s)} = 0 , \tag{A.44}$$

$$\sigma_{r\theta}{}^{(i)} + \sigma_{r\theta}{}^{(s)} = 0 . \tag{A.45}$$

Analogously, the coefficients A_m and B_m are determined from the simplified linear system of equations

$$\begin{pmatrix} S_{11} & S_{12} \\ S_{21} & S_{22} \end{pmatrix} \begin{pmatrix} A_m \\ B_m \end{pmatrix} = \frac{-1}{k_l^{(i)}} (-i)^{m+1} (2m+1) \begin{pmatrix} f_1 \\ f_2 \end{pmatrix} , \tag{A.46}$$

where

$$S_{11} = -\left[m^2 - m - \frac{(k_s^{(i)} a)^2}{2} \right] h_m(k_l^{(i)} a) - 2 \left[k_l^{(i)} a \right] h_{m+1}(k_l^{(i)} a) , \tag{A.47}$$

$$S_{12} = m(m+1)[(m-1) h_m(k_s^{(i)} a) - (k_s^{(i)} a) h_{m+1}(k_s^{(i)} a)] , \tag{A.48}$$

$$S_{21} = [m-1]\, h_m(k_l^{(i)} a) - \left[k_l^{(i)} a \right] h_{m+1}(k_l^{(i)} a) , \tag{A.49}$$

$$S_{22} = -\left[m^2 - 1 - \frac{(k_s^{(i)} a)^2}{2} \right] h_m(k_s^{(i)} a) - \left[k_s^{(i)} a \right] h_{m+1}(k_s^{(i)} a) , \tag{A.50}$$

and

$$f_1 = -\left[m^2 - m - \frac{(k_s^{(i)} a)^2}{2} \right] j_m(k_l^{(i)} a) - 2 \left[k_l^{(i)} a \right] j_{m+1}(k_l^{(i)} a) , \tag{A.51}$$

$$f_2 = [m-1]\, j_m(k_l^{(i)} a) - \left[k_l^{(i)} a \right] j_{m+1}(k_l^{(i)} a) . \tag{A.52}$$

The sacttering cross section γ^{sca} is then defined as

$$\gamma^{sca} = \frac{4\pi}{Re\left\{ k_l^{(i)} \right\}} Im \left\{ \sum_{m=0}^{\infty} i^m A_m \right\} . \tag{A.53}$$

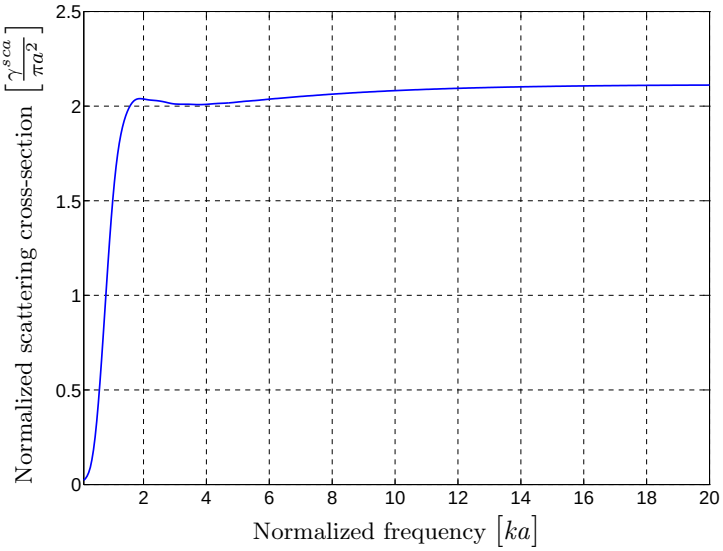

Figure A.1: Normalized scattering cross-section for a cavity in cement paste

The normalized scattering cross-section for a scattering cavity embedded in a cement paste matrix is depicted in Figure A.1.

A.2 Three-phase EMT Model

In order to model a three phase material consisting of a matrix material including elastic obstacles of spherical shape as well as spherical cavities, the EMT model proposed by Sabina and Willis [30] and described in Chapter 3 can be extended.

The matrix material, which can show a viscoelastic behavior, is defined by the elastic constants $\tilde{\kappa}_{\mathrm{M}}$, $\tilde{\mu}_{\mathrm{M}}$ and the density ρ_{M}, while the elastic inclusions are defined by the elastic constants κ_{Inc}, μ_{Inc} and density ρ_{Inc}. The inclusion parameters for the air voids are assumed to be zero since no wave propagation is possible in the cavities.

In order to find the overall effective material parameters, Eqs. 3.5 - 3.7, need to be expanded by a summation term representing the additional material phase. These

expanded formulae are

$$\tilde{\kappa}_{\mathrm{EM}} = \tilde{\kappa}_{\mathrm{M}} + \frac{\eta\, h_{\mathrm{Inc}}(\tilde{k})h_{\mathrm{Inc}}(-\tilde{k})(\kappa_{\mathrm{Inc}} - \tilde{\kappa}_{\mathrm{M}})}{1 + 3\epsilon_{\mathrm{Inc,L}}\frac{\kappa_{\mathrm{Inc}} - \tilde{\kappa}_{\mathrm{EM}}}{3\tilde{\kappa}_{\mathrm{EM}} + 4\tilde{\mu}_{\mathrm{EM}}}} + \frac{\phi\, h_{\mathrm{Air}}(\tilde{k})h_{\mathrm{Air}}(-\tilde{k})(-\tilde{\kappa}_{\mathrm{M}})}{1 + 3\epsilon_{\mathrm{Air,L}}\frac{-\tilde{\kappa}_{\mathrm{EM}}}{3\tilde{\kappa}_{\mathrm{EM}} + 4\tilde{\mu}_{\mathrm{EM}}}}\,, \quad \text{(A.54)}$$

$$\begin{aligned}\tilde{\mu}_{\mathrm{EM}} = \tilde{\mu}_{\mathrm{M}} &+ \frac{\eta\, h_{\mathrm{Inc}}(\tilde{k})h_{\mathrm{Inc}}(-\tilde{k})(\mu_{\mathrm{Inc}} - \tilde{\mu}_{\mathrm{M}})}{1 + 2(\mu_{\mathrm{Inc}} - \tilde{\mu}_{\mathrm{EM}})\frac{2\epsilon_{\mathrm{Inc,L}}\tilde{\mu}_{\mathrm{EM}} + \epsilon_{\mathrm{Inc,S}}(3\tilde{\kappa}_{\mathrm{EM}} + 4\tilde{\mu}_{\mathrm{EM}})}{5\tilde{\mu}_{\mathrm{EM}}(3\tilde{\kappa}_{\mathrm{EM}} + 4\tilde{\mu}_{\mathrm{EM}})}} \\ &+ \frac{\phi\, h_{\mathrm{Air}}(\tilde{k})h_{\mathrm{Air}}(-\tilde{k})(-\tilde{\mu}_{\mathrm{M}})}{1 + 2(-\tilde{\mu}_{\mathrm{EM}})\frac{2\epsilon_{\mathrm{Air,L}}\tilde{\mu}_{\mathrm{EM}} + \epsilon_{\mathrm{Air,S}}(3\tilde{\kappa}_{\mathrm{EM}} + 4\tilde{\mu}_{\mathrm{EM}})}{5\tilde{\mu}_{\mathrm{EM}}(3\tilde{\kappa}_{\mathrm{EM}} + 4\tilde{\mu}_{\mathrm{EM}})}}\,,\end{aligned} \quad \text{(A.55)}$$

$$\tilde{\rho}_{\mathrm{EM}} = \rho_{\mathrm{M}} + \frac{\eta\, h_{\mathrm{Inc}}(\tilde{k})h_{\mathrm{Inc}}(-\tilde{k})(\rho_{\mathrm{Inc}} - \rho_{\mathrm{M}})}{1 + (\rho_{\mathrm{Inc}} - \rho_{\mathrm{EM}})\frac{3 - \epsilon_{\mathrm{L}} - 2\epsilon_{\mathrm{S}}}{3\tilde{\rho}_{\mathrm{EM}}}} + \frac{\phi\, h_{\mathrm{Air}}(\tilde{k})h_{\mathrm{Air}}(-\tilde{k})(-\rho_{\mathrm{M}})}{1 + (-\rho_{\mathrm{EM}})\frac{3 - \epsilon_{\mathrm{Air,L}} - 2\epsilon_{\mathrm{Air,S}}}{3\tilde{\rho}_{\mathrm{EM}}}}\,, \quad \text{(A.56)}$$

where $h_{\mathrm{Inc}}(\tilde{k})$, $h_{\mathrm{Air}}(\tilde{k})$, $\epsilon_{\mathrm{Inc,L}}$ and $\epsilon_{\mathrm{Air,L}}$ have to be chosen according to the respective inclusion type and size.

Once the effective material parameters $\tilde{\kappa}_{\mathrm{EM}}$, $\tilde{\mu}_{\mathrm{EM}}$ and $\tilde{\rho}_{\mathrm{EM}}$ for the particulate material are found, the resulting attenuation coefficient is calculated following the steps described in Chapter 3.

REFERENCES

[1] Achenbach, J., *Wave Propagation in Elastic Solids*, vol. 16 of *Applied Mathematics and Mechanics*. Elsevier Science Publishers B.V., 1975.

[2] Becker, J., *Investigation of the Microstructure of Heterogeneous Materials Using Ultrasonic Waves*. Georgia Institute of Technology, Master Thesis, 2002.

[3] Biwa, S., "Independent scattering and wave attenuation in viscoelastic composites," *Mechanics of Materials*, vol. 33, pp. 635–647, 2001.

[4] Brauner, N. and Beltzer, A., "Wave-obstacle interaction in a lossy medium: energy perturbations and negative extinction," *Ultrasonics*, vol. 26, pp. 328–334, 1988.

[5] Cheeke, J., *Fundamentals and Applications of Ultrasonic Waves*. CRC Press, 2002.

[6] Frey, A., Coppens, A., and Sanders, J., *Fundamentals of Acoustics*. John Wiley & Sons, 3^{rd} ed., 1982.

[7] Graff, K., *Wave Motion in Elastic Solids*, vol. 16 of *Applied Mathematics and Mechanics*. Dover Publications, 1975.

[8] Hartmann, B. and Jarzynski, J., "Ultrasonic hysteresis absorption in polymers," *Journal of Applied Physics*, vol. 43, pp. 4304–4312, 1972.

[9] Hutchins, D. and Hayward, G., "The radiated field of ultrasonic transducers," *Physical Acoustics*, vol. 19, 1990.

[10] Jacobs, L. and Owino, J., "Effect of aggregate size on attenuation of Rayleigh surface waves in cement-based materials," *Journal of Engineering Mechnanics*, vol. 126, pp. 1124–1130, 2001.

[11] Kanaun, S., Lavin, V., and Sabina, F., "Propagation of elastic waves in composites with random set of spherical inclusions (effective medium approach)," *Wave Motion*, vol. 40, pp. 69–88, 2004.

[12] Kim, J.-Y., "Antiplane shear wave propagation in fiber-reinforced composites," *Journal of the Acoustical Society of America*, vol. 113, pp. 2442–2445, 2003.

[13] Kim, J.-Y., "Extinction of elastic wave energy due to scattering in a viscoelastic medium," *Int. Journal of Solids and Structures*, vol. 40, 2003.

[14] Kim, J.-Y., Ih, J., and Lee, B., "Dispersion of elastic waves in random particulate composites," *Journal of the Acoustical Society of America*, vol. 97, pp. 1380–1388, 1995.

[15] Kurtis, K., Collins, C., and Monteiro, P., "The surface chemistry of the alkali-silica reaction: A critical evaluation and x-ray microscopy," *RILEM Concrete Science and Engineering*, 2002.

[16] Lavrentyev, A. and Rokhlin, S., "Ultrasonic spectroscopy of imperfect contact interfaces between a layer and two solids," *Journal of the Acoustical Society of America*, 2006.

[17] Levenberg, K., "A method for the solution of certain problems in least-squares," *Quarterly applied mathematics*, vol. 2, pp. 164–168, 1944.

[18] Maess, J., *Attenuation Models for Material Characterization.* Georgia Institute of Technology, Master Thesis, 2004.

[19] Monteiro, P., *Concrete - Microstructure, Properties and Materials*. McGraw-Hill, 3^{rd} ed., 2006.

[20] Morse, P. and Ingard, K., *Theoretical Acoustics*. McGraw-Hill, 1968.

[21] Nadeau, J., "Water cement ratio gradients in mortars and corresponding effective elastic properties," *Cement and Concrete Research*, vol. 32, pp. 481–490, 2002.

[22] Oppenheim, A. and Schafer, R., *Discrete-time Signal Processing*. Prentice Hall, 1999.

[23] Owino, J. and Jacobs, L., "Attenuation measurements in cement-based materials using laser ultrasonics," *Journal of Engineering Mechnanics*, vol. 125, pp. 637–647, 1999.

[24] Pezant, J., *High Temperature Thickness Monitoring Using Ultrasonic Waves*. Georgia Institute of Technology, Master Thesis, 2008.

[25] Punurai, W., *Cement-based Materials' Characterization Using Ultrasonic Attenuation*. Georgia Institute of Technology, Ph.D. Dissertation, 2006.

[26] Punurai, W., Jarzynski, J., Qu, J., Kim, J.-Y., Jacobs, L., and Kurtis, K., "Characterization of mulit-scale porosity in cement paste by advanced ultrasonic techniques," *Cement and Concrete Research*, vol. 37, pp. 38–46, 2007.

[27] Punurai, W., Jarzynski, J., Qu, J., Kurtis, K., and Jacobs, L., "Characterization of entrained air voids with scattered ultrasound," *NDT & E Int. 39*, pp. 514–524, 2006.

[28] Rogers, P. and Van Buren, A., "An exact expression for the lommel diffraction correction integral," *Journal of the Acoustical Society of America*, vol. 55, pp. 724–728, 1974.

[29] Rose, J., "Ultrasonic waves in solid media," *Cambridge University Press*, 1999.

[30] Sabina, F. and Willis, J., "A simple self-consistent analysis of wave propagation in particulate composites," *Wave Motion*, vol. 10, pp. 127–142, 1988.

[31] Sears, F. and Bonner, B., "Ultrasonic attenuation measurement by spectral ratios utilizing signal processing techniques," *IEEE Transactions on Geoscience and Remote Sensing*, vol. GE-19, pp. 95–99, 1981.

[32] Shah, S., Popovics, J., Subramanian, K., and Aldea, C., "New directions in concrete health monitoring technology," *Journal of Engineering Mechanics*, vol. 126, pp. 754–760, 2000.

[33] Tharmaratnam, K. and Tan, B., "Attenuation of ultrasonic pulse in cement mortar," *Cement and Concrete Research*, vol. 20, 1990.

[34] Waterman, P. and Truell, R., "Multiple scattering of waves," *Journal of Mathematical Physics*, vol. 2, pp. 512–537, 1961.

[35] Ying, C. and Truell, R., "Scattering of a plane longitudinal wave by a spherical obstacle in an isotropically elastic solid," *Journal of Applied Physics*, vol. 27, pp. 1086–1097, 1956.

[36] Zhang, J., B.Drinkwater, and Dwyer-Joyce, R., "Acoustic measurement of lubricant-film thickness distribution in ball bearings," *Journal of the Acoustical Society of America*, 1998.